



Sulfamethoxazole degradation by regulating active sites on distilled spirits lees-derived biochar in a continuous flow fixed bed peroxymonosulfate reactor

Yanshan Wang^a, Wenzhao Peng^b, Jun Wang^b, Guanyi Chen^{a,c,d}, Ning Li^{a,d,*}, Yingjin Song^a, Zhanjun Cheng^{a,*}, Beibei Yan^a, Li'an Hou^a, Shaobin Wang^e

^a School of Environmental Science and Engineering, Tianjin University/Tianjin Key Lab of Biomass/Wastes Utilization, Tianjin 300072, PR China

^b Department of Chemical Engineering, Tianjin University, Tianjin 300350, PR China

^c School of Mechanical Engineering, Tianjin University of Commerce, Tianjin 300134, PR China

^d Georgia Tech Shenzhen Institute, Tianjin University, Shenzhen 518071, PR China

^e School of Chemical Engineering and Advanced Materials, The University of Adelaide, Adelaide SA 5005, Australia

ARTICLE INFO

Keywords:

Biochar
Peroxymonosulfate
Continuous flow fixed bed reactor
Active sites
Synergistic contribution

ABSTRACT

Defect type and interactions among active sites are critical in heterogeneous peroxymonosulfate (PMS) system. Herein, a continuous flow fixed bed PMS reactor with distilled spirits lees derived biochar (DSLBS)/quartz wool was designed to explore the synergistic roles of active sites. Satisfyingly, with high graphite N, C=O content and defect degree, DSLB-800 exhibited superior catalytic activity, durability and applicability for sulfamethoxazole (SMX) removal. The dominant contribution of $^1\text{O}_2$, and minor roles of $\text{SO}_4^{\bullet-}$ and $\bullet\text{OH}$ were confirmed. Single graphite N, C=O and C-O, combined interactions between graphite N and pyridine N, graphite N and pyrrole N, pyridine N and pyrrole N, C=O and O=C-O, O=C-O and C-O, as well as interactions among graphite N, pyridine N and pyrrole N contributed to $^1\text{O}_2$ generation. Notably, the double vacancy defect was also a preferential site for $^1\text{O}_2$ production. This study advances mechanistic understanding of collaborative contribution of active sites to PMS activation.

1. Introduction

Peroxymonosulfate-based advanced oxidation (PMS-AO) is a promising approach for the degradation of recalcitrant organic pollutants from wastewater due to wide adaptable pH range, strong and selective oxidation capability [1–4]. Currently, the PMS-AO has aroused great concern for antibiotics decontamination [5]. The non-radical mediated oxidation pathway could dominate by regulating reactive oxygen species (ROS) in PMS system [6]. The non-radical species were not sensitive to co-existing organic matter and ions, strengthening the application potential of PMS-AO in practical water treatment.

Commonly, catalysts play a critical role in PMS activation. Various types of catalysts have been reported, including transition metals (e.g. Co, Fe, Cu, Mn, Al) [7,8], metal oxides (e.g. CuO , Fe_2O_3) [9,10], carbon (e.g. graphene, carbon nanotubes, nano diamonds) [11–13], biochar-based catalysts [3,14–17] and carbon loaded with metal [18,19]. However, the metal-based catalysts face several limitations, such as

high cost, possible leaching of toxic metals, and inconvenient separation and recovery of homogeneous metal catalysts [8,13,20]. Comparatively, the carbon catalysts exhibit low contamination potential and excellent thermal stability. Biochar-based catalysts are prepared easily by thermal decomposition of sludge, manure, agricultural and forestry waste, and so on [21–23]. The biochar has received growing interest for PMS activation owing to the extensive resource, high porous structure and inherent functional sites [16,24,25]. Previous reports have shown that the distribution of active sites on catalyst surface affects ROS generation in PMS system [3,26]. Rational regulation of the type and concentration of ROS are beneficial to achieve selective and efficient removal of target pollutants.

Currently, most PMS systems have been limited at sequential batch scale, which mainly concentrate on catalyst activity and related mechanisms [22,27,28]. Interestingly, the continuous flow reactors appear convenient in the practical applications of PMS-AO [29]. To the best of our knowledge, few study has been focused on optimization of

* Correspondence to: No.135, Yaguan Road, Jinnan District, Tianjin City, PR China.

E-mail addresses: liningec@tju.edu.cn (N. Li), zjcheng@tju.edu.cn (Z. Cheng).

<https://doi.org/10.1016/j.apcatb.2022.121342>

Received 18 December 2021; Received in revised form 6 March 2022; Accepted 20 March 2022

Available online 24 March 2022

0926-3373/© 2022 Elsevier B.V. All rights reserved.

influencing factors, regulation of ROS and selective degradation of pollutants in a continuous flow fixed bed PMS reactor. Particularly, the actual exposure of active sites on the catalyst surface remains elusive in continuous flow reactors. Especially, the collaborative contribution of different sites to PMS activation is unclear, impeding developments of PMS-AO techniques in water treatment process.

Distilled spirits lees (DSL), an inevitable by-product in spirits production process [30], was selected as a potential feedstock for biochar preparation due to the rich lignocellulose and low heavy metal content. Besides, the quartz wool was chosen as carrier for biochar-based catalysts in a fixed bed PMS reactor. Importantly, the collaborative contribution of different active sites to PMS activation was revealed for the first time in a continuous flow fixed bed reactor. The dominant defect type for PMS activation to produce $^1\text{O}_2$ was identified via DFT calculation. The goals of this work were to 1) investigate the physicochemical properties of DSLBs with different preparation temperatures (500–800 °C); 2) evaluate the activity of DSLBs in a continuous flow fixed bed PMS reactor; 3) regulate active sites on DSLBs to produce highly efficient active species in PMS system; 4) propose mechanisms of sulfamethoxazole (SMX) oxidation through DFT calculations combined with correlation analysis. This study provided a feasible strategy for DSL utilization and a continuous flow fixed bed PMS reactor for SMX degradation. The results shed new lights on active sites effects in the process of pollution degradation in continuous PMS-AO system.

2. Materials and methods

2.1. Chemicals

The details of the chemical reagents were provided in the Text S1 of [Supporting Information \(SI\)](#).

2.2. Sources of DSL and biochar preparation

DSL was provided from a winery in Kweichow, China. The obtained DSL was dried to constant weight at 105 °C and then crushed and sieved. The sample with particle size less than 0.45 mm was selected as feedstock for biochar preparation.

The DSL with mass of 10 g was transferred into a tube furnace for thermal treatment. The treatment process lasted 2 h at 500 °C, 600 °C, 700 °C and 800 °C (heating rate of 10 °C/min) under N_2 atmosphere and the samples were labeled as DSLB-500, DSLB-600, DSLB-700 and DSLB-800, respectively.

2.3. Characterization of DSLBs

Details of DSLBs characterization were given in Text S2 of SI.

2.4. DSLBs activity test in fixed bed PMS reactor

The schematic diagram of the reactor was shown in [Fig. 1](#), the prepared DSLBs were loaded in a fixed-bed PMS reactor with an effective volume of 100 mL for SMX oxidation. Specifically, a certain amount of mixed solution with PMS and SMX was stirred at 25 °C. Afterward, DSLBs were dispersed in mixed solution and then the quartz wool was submerged, making the catalyst being coated uniformly. Then, the quartz wool loaded with DSLBs was packed into the reactor. The mixed solution was pumped into the reactor with a flow rate of 3.6 mL/min for 2 h. Furthermore, the biochar-loaded continuous flow fixed bed PMS reactor was prepared for SMX adsorption in the absence of PMS.

The effects of DSLBs dose, PMS concentration, solution pH and co-existing ions have been examined in a continuous flow fixed bed PMS reactor. To further confirm the durability of DSLBs, 1 L of SMX solution was treated by the fixed bed reactor in a continuous operation mode. About 1.0 mL sample was extracted from the influent and effluent at regular intervals and filtered through a 0.22 μm membrane. Excess

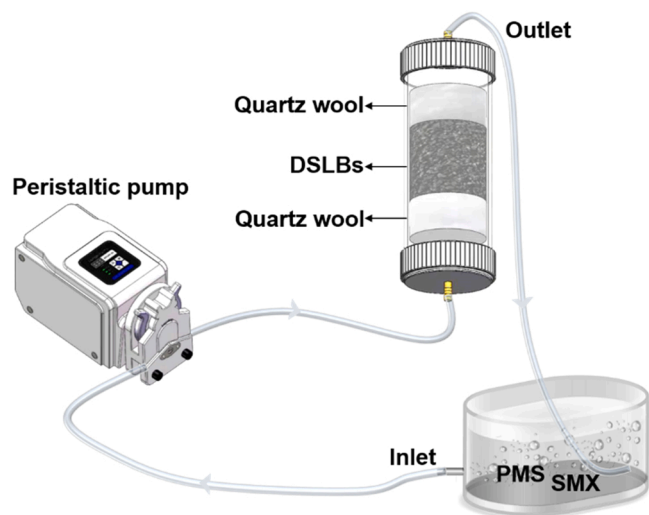


Fig. 1. The schematic diagram of the continuous flow fixed bed PMS reactor.

$\text{Na}_2\text{S}_2\text{O}_3$ was employed to quench the reaction. Subsequently, the concentration of SMX in the mixture was measured by high-performance liquid chromatograph (HPLC, 2030 C, Shimadzu) with a C18 column and a UV detector at 264 nm. The mobile phase and gradient elution procedures referred to our previous studies [3,6]. Additionally, the ROS in DSLBs/PMS system were identified using different quenching agents such as TBA (500 mM), EtOH (500 mM), p-BQ (30 mM) and L-histidine (30 mM). Electron paramagnetic resonance (EPR, E 500, Bruker) spectroscopy was employed to detect ROSs such as $^{\bullet}\text{OH}$, $\text{SO}_4^{\bullet-}$, $\text{O}_2^{\bullet-}$, and $^1\text{O}_2$ species during SMX degradation. The degradation intermediates of SMX were detected by high performance liquid chromatograph (HPLC, Ultimate 3000, Thermo Scientific) coupled to mass spectrometry (MS, Q Exactive, Thermo Scientific).

2.5. DFT calculations

All model calculations were conducted based on the density functional theory (DFT) using projected augment wave method as implemented in the Vienna ab initio Simulation Package (VASP) code. The adsorption of PMS on defect-carbon was simulated using a (8×8) supercell with a vacuum layer of 20 Å. A k-mesh of $2 \times 2 \times 1$ was used for the sampling of Brillouin-zone. The atoms were relaxed fully until the force acting on each atom was less than 0.02 eV/Å. Van der Waals (vdW) interaction was taken into account at the DFT-D2 level. Details of the DFT calculation was provided in Text S3 of SI.

3. Results and discussion

3.1. Characteristics and activity of DSLBs

The morphology and microstructure of DSLBs were shown in [Fig. 2](#). Clearly, the morphology was influenced by calcination temperature. DSLB-500 sample exhibited a relatively smooth and denser structure, preserving the inherent morphology of DSL fibers ([Fig. 2a](#)). The inherent morphology of DSL was disrupted as the temperature increased, forming honeycomb-like pore and channel structure in DSLB-600 ([Fig. 2b](#)). However, the excessive temperature caused the collapse of pore and channel structure in DSLB-700 and DSLB-800 ([Figs. 2c and 2d](#)), which was well confirmed by the BET results ([Table 1](#)). The specific surface area (SSA) and total porous volume of DSLB-600 were 190.22 $\text{m}^2 \text{g}^{-1}$ and 0.13 $\text{cm}^3 \text{g}^{-1}$, which were much higher than those of other DSLBs. The average pore diameter of DSLB-800, DSLB-700, DSLB-600 and DSLB-500 were 3.27, 21.43, 18.34 and 22.96 nm, respectively. The mesopores (3.27 nm) were formed at 800 °C due to C skeleton collapse

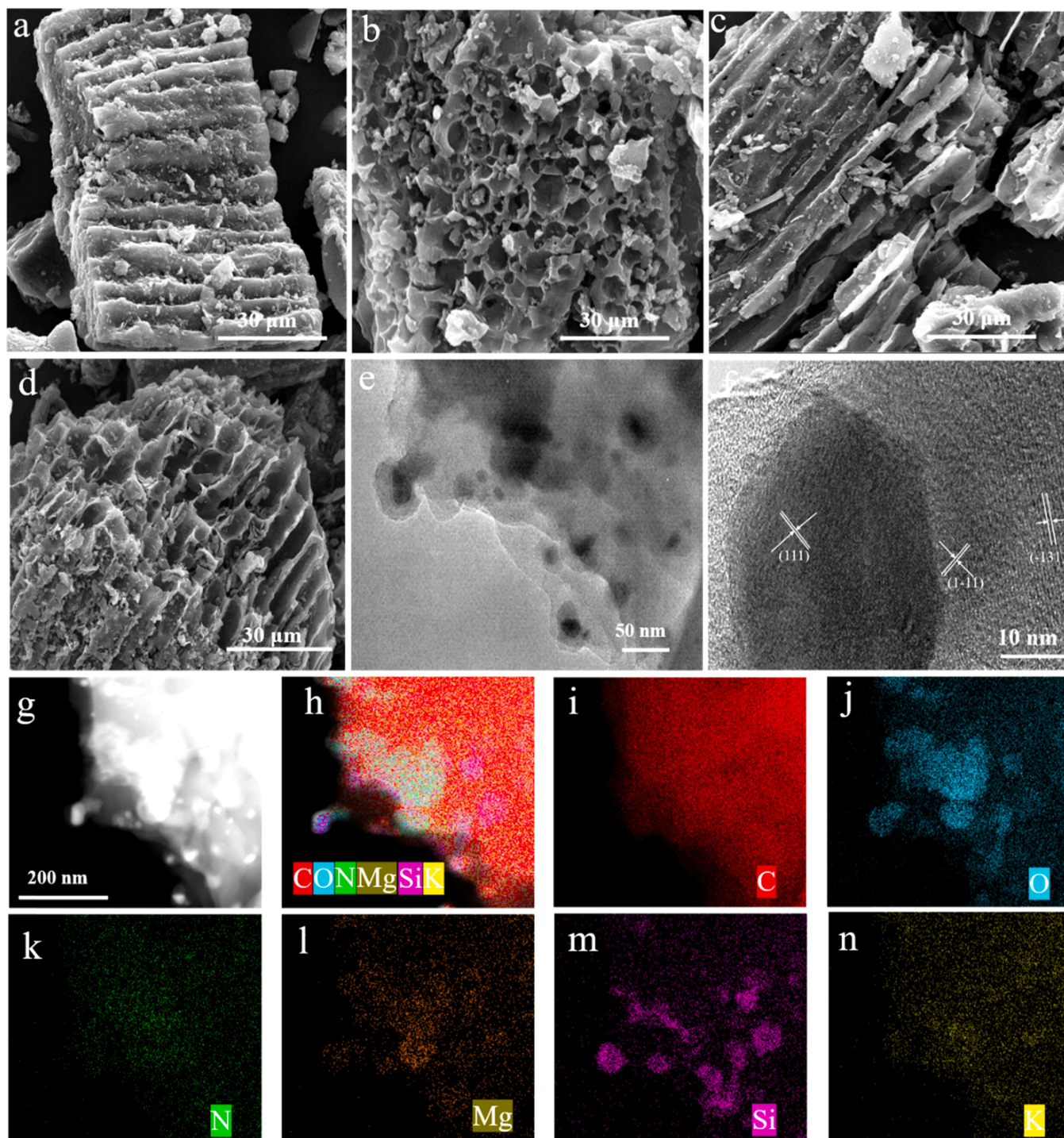


Fig. 2. SEM images of (a) DSLB-500, (b) DSLB-600, (c) DSLB-700 and (d) DSLB-800; (e) TEM and (f) HRTEM images of DSLB-800; (g) High-angle-annular-dark-field scanning transmission electron microscopy (HAADF -STEM) image of DSLB-800 and (h) corresponding EDS mapping images of DSLB-800: (i) C, (j) O, (k) N, (l) Mg, (m) Si and (n) K elements.

by decomposition and conversion of amorphous carbon into dense graphitic carbon [31]. Generally, mesopores and appropriate SSA were conducive to more reactive site exposure without disrupting electron transfer [32]. Hence, the DSLB-800 was endowed with great potential for activating PMS to degrade contaminants.

Additionally, some irregular rough small bumps were embedded on the surface of samples. The similar phenomenon was also found in the TEM images of DSLB-800 (Fig. 2e). Some regular lattice fringes with spacing of 0.243, 0.309 and 0.280 nm were obtained in the HRTEM

images of DSLB-800 (Fig. 2f), assigning to the (111) plane of MgO, (-131) plane of tilleyite and ($1-11$) plane of phosphogartrellite, respectively. The C, O, N, Si, Mg and K elements were distributed uniformly in DSLB-800 according to the EDS-mapping images (Fig. 2g-n).

The crystalline phases of DSLBs samples were revealed by XRD patterns in Fig. 3a. The broad diffraction peak around $2\theta = 26.0^\circ$ were identified in all DSLBs, suggesting the amorphous features of carbon structure in biochar [32]. Obviously, two distinct diffraction peaks could be observed at 26.6° and 44.3° with calcination temperature increasing

Table 1
Specific surface area and pore structure of DSLBs.

Samples	Specific surface area (m ² /g)	Average pore diameter (nm)	Total pore volume (cm ³ /g)
DSL-500	75.90	22.96	0.076
DSL-600	190.22	18.34	0.130
DSL-700	79.04	21.43	0.073
DSL-800	76.78	3.27	0.079

to 700 °C and 800 °C, corresponding to (002) and (100) planes of graphitic carbon (JCPDS PDF#26-1079), respectively [3,6,31,32]. The improved graphitization degree at high temperature implied better electronic properties [33–35]. Besides, the weak peak at 36.9° was identified as (111) plane of MgO (JCPDS PDF#45-0946). The other two peaks at 28.8° and 31.8° matched well with the (−131) and (1−11) lattice planes of tilleyite and phosphogartrellite (JCPDS PDF#45-0946 and 51-1449), respectively. The crystalline mineral peaks might be converted from impurities in the lignocellulose-rich biomass.

The surface functional groups in DSLBs were also analyzed by FTIR spectroscopy (Fig. 3b). Two typical peaks were clearly observed at 3432 and 1382 cm^{−1}, ascribing to stretching vibrations of O-H and C-C. The 2921 and 2855 cm^{−1} peaks corresponded to stretching vibrations of -CH₂ in alkyl [23]. Another two characteristic peaks locating at 1629 cm^{−1} and 1070 cm^{−1} were belonged to aromatic C=O and C-O-C stretching vibration in lignin and cellulose of DSLBs [36]. Furthermore, the evident peak at 797 cm^{−1} was attributed to the out-of-plane vibration of aromatic C-H in cellulose and carbohydrates [37]. Remarkably,

the peak intensity of O-H and C-O-C stretching vibration weakened significantly with the increase of pyrolysis temperature owing to the loss of various oxygen-containing groups.

The defect degree of DSLBs was calculated according to Raman spectra (Fig. 3c). In general, the D band (1340 cm^{−1}) and G band (1590 cm^{−1}) were considered as defects in the carbon atomic crystal and plane stretching motion of sp² carbon atoms, respectively [38]. The higher intensity ratio of D and G band (I_D/I_G) referred to higher degree of defects in DSLBs. Clearly, the value of I_D/I_G raised gradually with preparation temperature. Specifically, the I_D/I_G value of DSLB-800 (0.927) was much higher than those of DSLB-700 (0.871), DSLB-600 (0.827) and DSLB-500 (0.812), indicating more defects in DSLB-800. Thus, the DSLB-800 might provide more active sites for PMS activation.

The chemical composition and active sites distribution in DSLBs were further investigated by XPS analysis. As displayed in Fig. 4a, the characteristic peaks of C, N and O elements were observed in the XPS survey of all DSLBs samples. In Fig. S1a, the high-resolution C 1 s spectrum of DSLB-800 was deconvoluted into four peaks at 284.6, 285.2, 286.3 and 288.7 eV, which were ascribed to C-C/C=C, C-N/C-O, C=O and COOH, respectively [39,40]. Noticeably, the total C content increased with the calcination temperature. As shown in Fig. 4b, the maximum C content (74.76 at%) with C-C/ C=C (34.54 at%) and C=O (21.71 at%) was obtained under the calcination temperature of 800 °C. Besides, the percentage of COOH (1.14 at%) and C-N/C-O (17.37 at%) in DSLB-800 was lower than those in DSLB-700 (2.23 and 17.94 at%), DSLB-600 (2.66 and 21.33 at%) and DSLB-500 (3.32 and 25.36 at%). It can be inferred that dehydration, decarboxylation and aromatization occurred during decomposition of lignocellulosic biomass under high temperature [41–43].

The O1s peak in Fig. S1b could be identified as C=O, O-C=O and

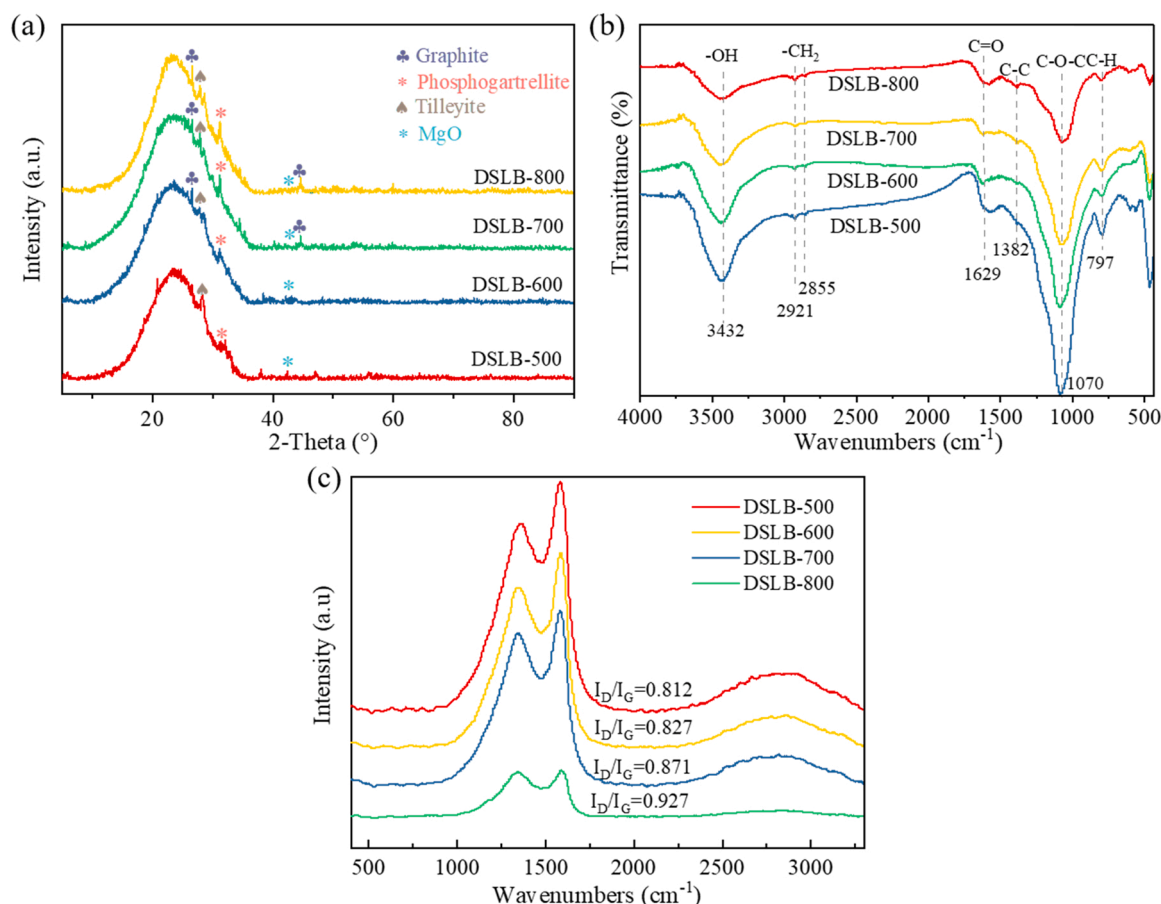


Fig. 3. (a) XRD spectra; (b) FTIR spectra; (c) Raman spectra of DSLBs prepared at various calcination temperatures.

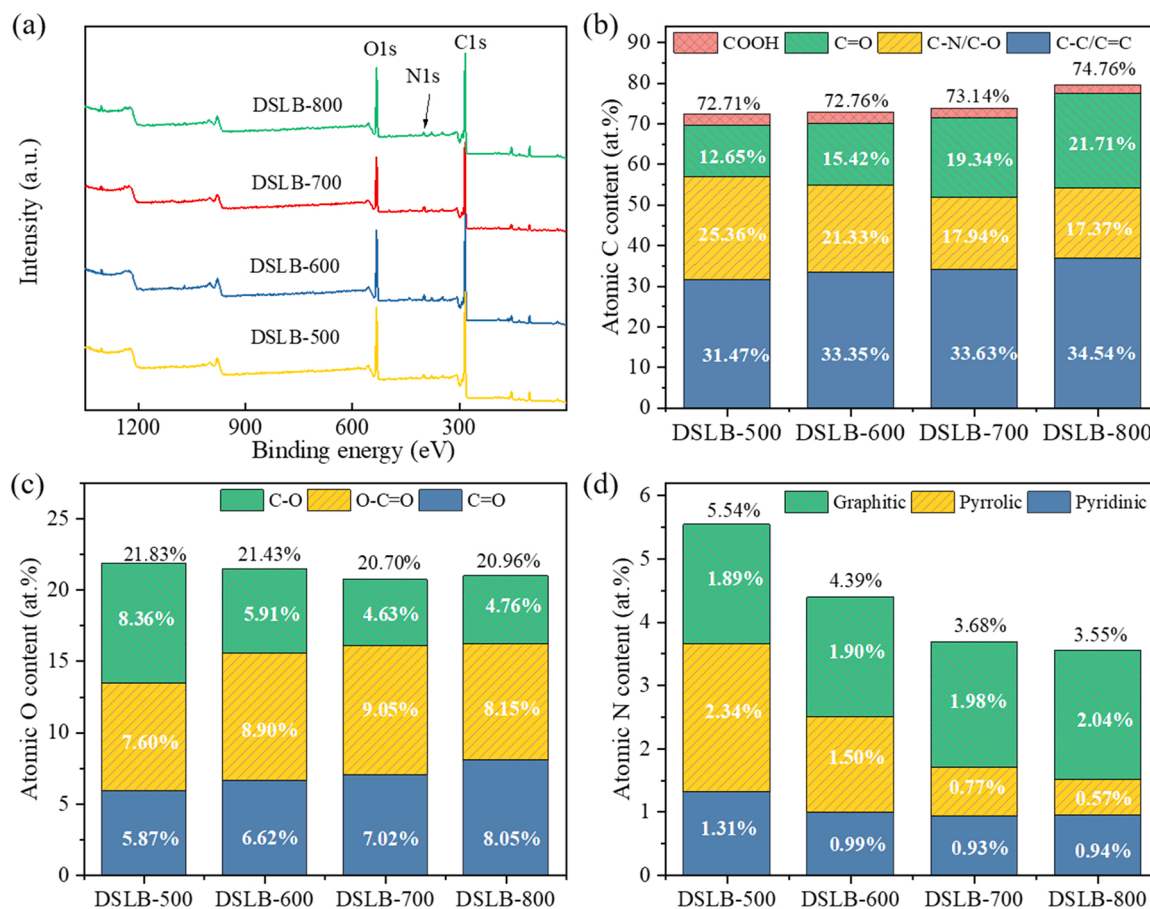


Fig. 4. XPS spectra of DSLBs (a) survey and corresponding contents of different active sites (b) C, (c) O and (d) N.

C=O groups at ~ 531.0 eV, ~ 532.6 eV and ~ 533.3 eV [44,45]. Similar to the C1s peak, the peak intensity of C=O in O1s also increased with calcination temperature. In particular, DSLB-800 was presented with the highest C=O content (8.05 at%), followed by DSLB-700 (7.02 at%), DSLB-600 (6.62 at%) and DSLB-500 (5.87 at%) (Fig. 4c). The increased C=O content was probably ascribed to the transformation of C-O group under high temperature, which would be conducive to $^1\text{O}_2$ generation during PMS activation [3,46]. As illustrated in Fig. S1c, the N1s spectra was divided into three peaks with binding energies of ~ 398.6 , ~ 399.8 and ~ 400.8 eV, representing pyridinic N, pyrrolic N and graphitic N, respectively. Clearly, the total N content decreased with increasing pyrolysis temperature from 500 °C to 800 °C (Fig. 4d). Some unstable nitrogen compounds were thermally decomposed during high temperature carbonization of DSLB [31]. Surprisingly, the pyrrole N and pyridine N content declined gradually with increasing calcination temperature, while the graphite N content increased from 1.89 at% at 500 °C to 2.04 at% at 800 °C. The elevated graphite N content might be result from its better thermal stability and conversion from pyrrole N and pyridine N [33]. As reported, graphitic N could conjugate the nitrogen lone pair electrons into deficient carbon atoms, which were more effective for PMS activation [32,47].

3.2. SMX degradation by PMS activation in a continuous flow fixed bed reactor

The performance of DSLBs on PMS activation was evaluated for SMX degradation in a continuous flow fixed bed reactor. As presented in Fig. S2, less than 3% of SMX removal was observed within 120 min by DSLBs adsorption. Consequently, the adsorption of SMX by the fixed bed reactor loaded with DSLBs alone was negligible. SMX degradation was

further performed by DSLBs activated PMS in a continuous flow fixed bed reactor. As presented in Fig. 5a, PMS alone presented a degradation efficiency of 60.1% within 120 min. The SMX removal was enhanced to 75.5% as PMS was activated by DSLB-500 in a continuous flow fixed bed reactor. Interestingly, the catalytic activity was enhanced gradually with the rise of pyrolysis temperature. Remarkably, the continuous flow fixed bed reactor packed with DSLB-800 exhibited excellent catalytic activity in the presence of PMS, achieving 96.9% degradation of SMX in 120 min. The superior catalytic activity of DSLB-800 might be ascribed to appropriate exposure of active sites at high temperature [3,6].

As shown in Fig. 5b, the SMX degradation data were fitted well with Langmuir-Hinshelwood (L-H) kinetics model (Eq. 1) with high correlation coefficients ($R^2 > 0.96$). The rate constants (k) increased from 0.0087 to 0.0299 min^{-1} with calcination temperature rising from 500 to 800 °C. More defects were formed under high temperature according to Raman results, which could provide more sites for accelerated PMS activation [48]. Besides, the DSLB-800 contained abundant graphite N and oxygen-containing functional groups (C=O and C-O-C), which also promoted the generation of reactive species from PMS [40]. Furthermore, the DSLB-800/PMS system achieved a satisfactory SMX removal efficiency of 86.7% in the actual effluent within 120 min, much higher than that with PMS alone (59.3%) (Fig. 5c). The DSLB-800 was feasible for PMS activation and actual wastewater treatment. To further confirm the application potential, the durability of the continuous flow fixed bed PMS reactor packed with DSLB-800 was evaluated by pumping 1 L of actual effluent with SMX in continuous mode for 20 h (Fig. 5d). A successive degradation of SMX was realized with a removal efficiency greater than 73.7%, indicating the degradation ability of the continuous flow fixed bed PMS reactor was stable.

$$\ln(C/C_0) = -k t \quad (1)$$

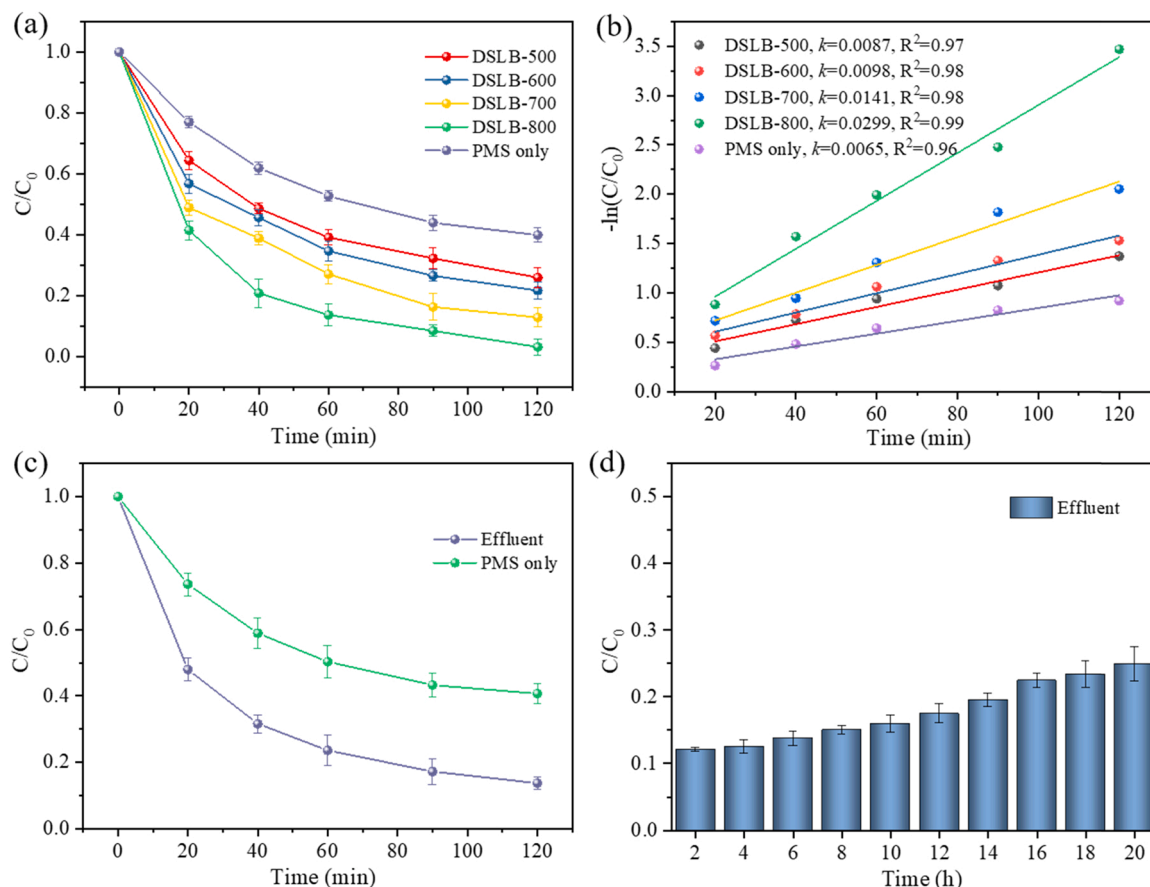


Fig. 5. (a) SMX degradation by DSLBs activated PMS in a continuous flow fixed bed reactor; (b) kinetic curves in different DSLBs/PMS systems fitted by pseudo-first-order kinetic model; (c) SMX degradation in practical effluent by DSLB-800 activated PMS in a continuous flow fixed bed reactor; (d) durability of the continuous flow fixed bed PMS reactor packed with DSLB-800 for SMX degradation. Experimental conditions: [DSLBS] = 2.0 g/L; [PMS]₀ = 2.5 mM; [SMX]₀ = 15.0 mg/L; pH = 5.24; T = 25 °C; flow rate (r) = 3.6 mL/min.

where t is the reaction time; k is the first-order kinetic constant; C_0 and C are SMX concentrations at the beginning and different reaction times, respectively.

Interestingly, the P2(C₄H₄N₂O₂), P4(C₁₀H₁₅N₃O₄S) and P8 (C₄H₆N₂O₄S) intermediates were detected during desorption experiment of the recovered DSLB-800 (Text S3, Fig S3, and Table S1). Thus, the slight decrease of SMX removal efficiency (from 86.7% to 73.7%) might be attributed to the adsorption of degradation intermediates, hindering PMS activation on catalyst surface. Besides, more clustered matter was found on the used DSLB-800 surface after reactions (Text S4, Fig S4). Meanwhile, variation in DSLB-800 surface chemistry before and after repeated cycles was clarified by XPS analysis (Text S4, Fig. S5). The decreased graphite N and C=O sites might be participated in PMS activation.

3.3. Effect of operation parameters on SMX degradation

3.3.1. Catalyst dosage, PMS concentration and solution pH

Considering the potential of practical applications, the operating parameters of DSLB-800/PMS system in a continuous flow fixed bed reactor were further optimized for rapid SMX degradation. The variation of SMX removal with different DSLB-800 dosages was displayed in Fig. 6a. As the DSLB-800 amounts increased from 0.5 to 1.0 g/L, the SMX removal efficiency elevated from 85.9% to 96.9% within 120 min. Correspondingly, the k value of SMX degradation raised gradually from 0.0142 to 0.0299 min⁻¹, implying that high DSLB-800 dosage provided more sites for PMS activation [35,49]. Likewise, the removal efficiency of SMX was also positively correlated with PMS concentration

($P < 0.05$). As displayed in Fig. 6b, about 37.5% of SMX ($k = 0.0026$ min⁻¹) was degraded in 120 min with 0.5 mM of PMS in a continuous flow fixed bed reactor loaded with DSLB-800. A noticeable improvement of SMX removal (96.9%) was observed when the PMS concentration increased to 2.5 mM. More oxide species could generate by taking full advantage of active sites on DSLB-800 with high concentration of PMS [6,50,51]. No significant inhibition of SMX degradation was observed in the presence of excess PMS. It can be inferred that $\text{SO}_4^{\bullet-}$ might not be the dominant oxide species for SMX degradation since excess $\text{SO}_4^{\bullet-}$ could also be scavenged by itself and form $\cdot\text{S}_2\text{O}_8^-$ by reacting with $\text{S}_2\text{O}_8^{2-}$ [50].

Degradation efficiency of SMX in different initial solution pH was presented in Fig. 6c. The DSLB-800/PMS in a continuous flow fixed bed reactor exhibited great adaptability in a wide initial pH range (3.0–9.0) for SMX removal. Specifically, almost more than 96% of SMX was degraded within 120 min at an initial pH of 2–7. Slight inhibition of SMX degradation was observed at pH = 9. Correspondingly, The k value at different pH media followed the order of pH = 3 (0.0321 min⁻¹) > pH = 5 (0.0299 min⁻¹) > pH = 7 (0.0146 min⁻¹) > pH = 9 (0.0142 min⁻¹). This trend was closely related to the surface charge of DSLB-800, and chemical speciation of SMX and PMS [3,35,50]. To further explain this phenomenon, the zeta potential of DSLB-800 at different solution pH was measured (Fig. 6d). The DSLB-800 surface is negatively charged at solution pH above 5.01 (pH_{ZPC} = 5.01), while SMX exists primarily in the anionic form at solution pH above 5.7 (pK_{a1} = 1.6; pK_{a2} = 5.7). As a result, charge repulsion in the relatively alkaline region and $\pi^+-\pi$ electron donor-acceptor interactions in the relatively acidic region were occurred, resulting in reduced removal of SMX under

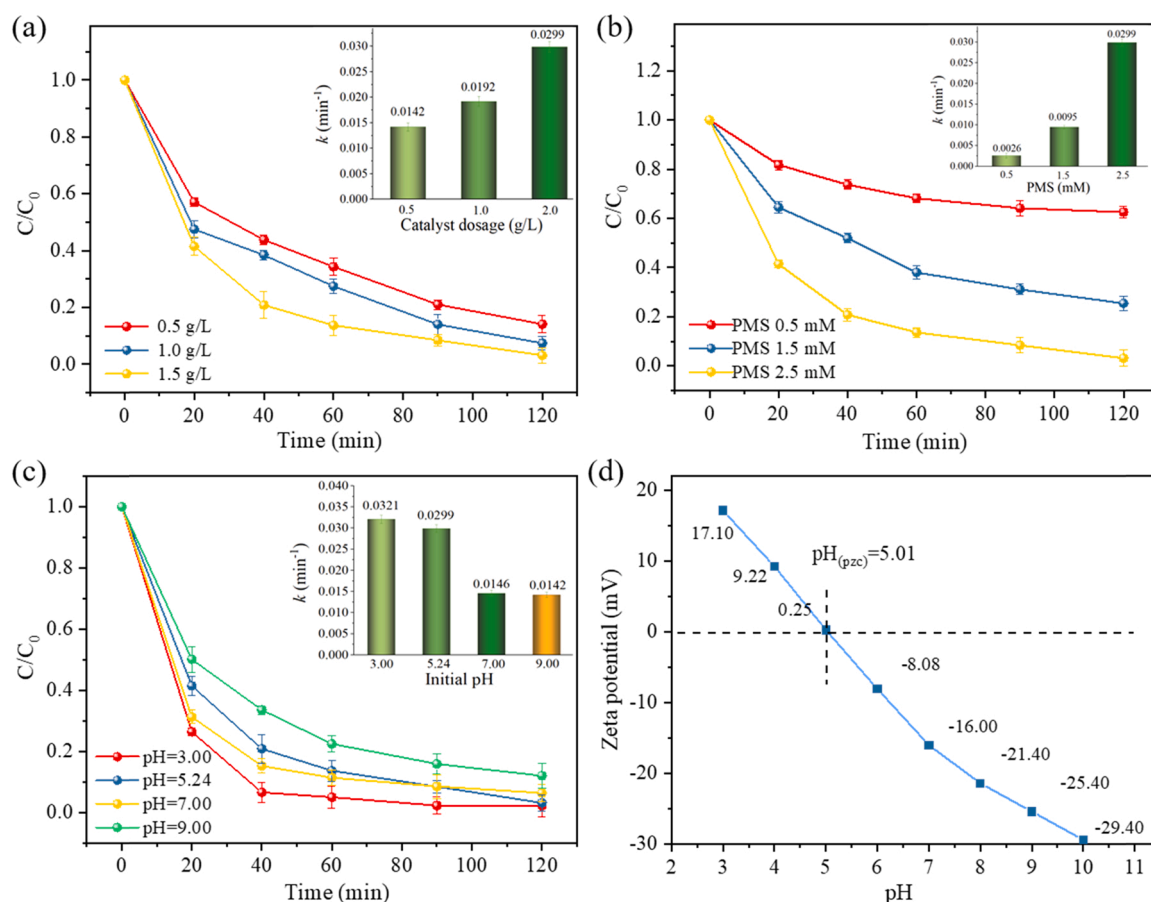


Fig. 6. Effect of (a) catalyst dosage, (b) PMS concentration and (c) initial solution pH on SMX removal in DSLB-800/PMS system with continuous flow mode (inset: corresponding apparent rate constants). Experimental conditions: [catalyst] = 2.0 g/L (except for a); [PMS]₀ = 2.5 mM (except for b); pH = 5.24 (except for c); [SMX]₀ = 15 mg/L; T = 25 °C; flow rate (r) = 3.6 mL/min; (d) Zeta potential of DSLB-800 as a function of pH.

alkaline conditions [35,52]. Notably, PMS presents mainly in the form of SO_5^{2-} with weak oxidizing capability under strongly alkaline conditions, which also poses negative impacts on the removal of negatively charged SMX [53,54].

3.3.2. Co-existing anions

To investigate the effects of co-existing anions and dissolved organic matter on SMX degradation in DSLB-800/PMS system, Cl^- , NO_2^- , SO_4^{2-} and humic acid (HA) were added into the continuous flow fixed bed

reactor, respectively. The corresponding variation of SMX concentration was shown in Fig. 7. Among these co-existing matrices, the NO_2^- , SO_4^{2-} and HA all have a negative effect on SMX degradation. The degradation efficiency of SMX decreased from 96.9% to 77.2%, 76.6% and 70.5%, respectively. Obviously, some PMS and active species were consumed by the co-existing substances.

Specifically, NO_2^- ($k = 0.0082 \text{ min}^{-1}$) exhibited a more potent inhibition than SO_4^{2-} ($k = 0.0145 \text{ min}^{-1}$), attributing to the easy oxidation of NO_2^- by hydroxyl radicals (Eq. 2 and Eq. 3) [51]. Besides, slight

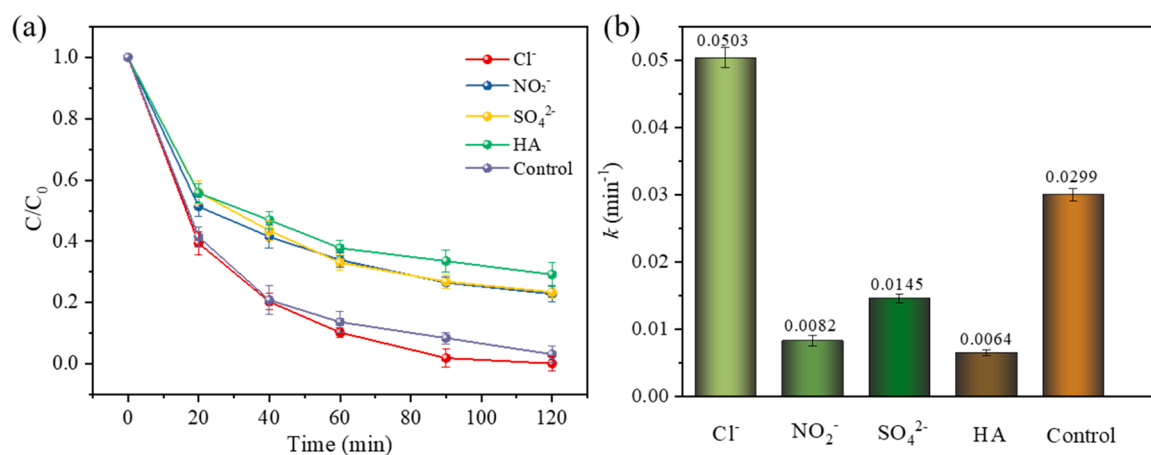
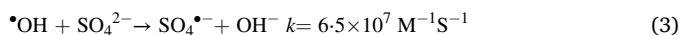
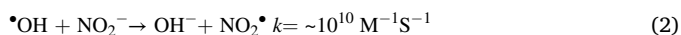
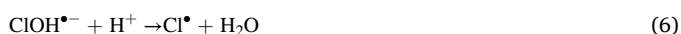


Fig. 7. (a) SMX degradation as a function of time; (b) pseudo-first-order kinetic constants with different inorganic anions and HA. Experimental conditions: [catalyst] = 2.0 g/L; [PMS]₀ = 2.5 mM; pH = 5.24; [SMX]₀ = 15.0 mg/L; T = 25 °C; flow rate (r) = 3.6 mL/min.

inhibition in the presence of SO_4^{2-} was attributed to reduced potential of E ($\text{SO}_4^{\bullet-}/\text{SO}_4^{2-}$) [55]. Regarding HA, as a typical organic interferent, the k value decreased from 0.0299 to 0.0064 min^{-1} . This inhibitory effect might result from the scavenging of reactive oxygen species by HA, hindering SMX degradation [56,57].



In contrast, SMX was almost degraded completely in the presence of Cl^- . The positive effect of Cl^- on SMX degradation could be explained in two aspects. On the one hand, the reaction between Cl^- and hydroxyl radicals leads to the generation of active chlorine species (Cl^{\bullet}) with high redox potential ($E^0(\text{Cl}^{\bullet}/\text{Cl}^-) = 2.4 \text{ V}$; $E^0(\text{Cl}_2^{\bullet-}/2\text{Cl}^-) = 2.1 \text{ V}$; $E^0(\text{Cl}_2/2\text{Cl}^-) = 1.4 \text{ V}$) (Eqs. 4–9), which could accelerate contaminants oxidation [49,58]. On the other hand, chlorine radicals mainly react with water to generate more hydroxyl radicals, thus achieving higher degradation efficiency [59].



3.4. Mechanism of PMS activation by DSLBs in a continuous flow fixed bed reactor

3.4.1. Identification of active species

To verify the generation of active species in DSLB-800/PMS system, EPR measurements were conducted. As demonstrated in Fig. 8a, two typical characteristic signals of $\text{DMPO} \cdot \bullet\text{OH}$ and $\text{DMPO} \cdot \text{SO}_4^{\bullet-}$ were identified in the system, confirming the presence of both $\bullet\text{OH}$ and $\text{SO}_4^{\bullet-}$ [47]. Besides, the signal intensity of $\text{DMPO} \cdot \bullet\text{OH}$ and $\text{DMPO} \cdot \text{SO}_4^{\bullet-}$ in EPR spectra increased gradually with the reaction time, revealing that DSLB-800 could activate PMS effectively and consistently [6]. Similarly, the weak intensity of $\text{TEMP} \cdot {}^1\text{O}_2$ signal was observed in sole PMS system, suggesting the minor role of PMS self-decomposition in ${}^1\text{O}_2$ generation. Noticeably, the strong signal peak of $\text{TEMP} \cdot {}^1\text{O}_2$ with an intensity ratio of 1:1:1 was observed in the presence of DSLB-800 (Fig. 8b), indicating that ${}^1\text{O}_2$ species were produced mainly by PMS activation with DSLB-800

catalyst [60]. Thus, $\bullet\text{OH}$, $\text{SO}_4^{\bullet-}$ and ${}^1\text{O}_2$ could generate by DSLB-800 activated PMS, which might contribute to SMX degradation.

3.4.2. Identification of ROS

Quenching experiments confirmed the presence of $\text{SO}_4^{\bullet-}$, $\bullet\text{OH}$ and ${}^1\text{O}_2$ in DSLBs/PMS systems (Text S6, Fig. S6). In order to evaluate the contributions of various reactive species in the DSLBs/PMS system more clearly, typical chemical probes were selected to discern different ROSs. Typically, Benzoic acid (BA) was used to detect the occurrence of $\bullet\text{OH}$ and $\text{SO}_4^{\bullet-}$ ($k_{(\bullet\text{OH}, \text{BA})} = 4.2 \times 10^9 \text{ M}^{-1} \text{ s}^{-1}$ and $k_{(\text{SO}_4^{\bullet-}, \text{BA})} = 1.2 \times 10^9 \text{ M}^{-1} \text{ s}^{-1}$) [61,62]. Nitrobenzene (NB) was widely used to identify $\bullet\text{OH}$ ($k_{(\bullet\text{OH}, \text{NB})} = 4.7 \times 10^9 \text{ M}^{-1} \text{ s}^{-1}$) [61,63]. Furfuryl alcohol (FFA) was often regarded as an effective chemical probe for detection of ${}^1\text{O}_2$ and $\bullet\text{OH}$ ($k_{({}^1\text{O}_2, \text{FFA})} = 1.2 \times 10^8 \text{ M}^{-1} \text{ s}^{-1}$ and $k_{(\bullet\text{OH}, \text{FFA})} = 1.5 \times 10^{10} \text{ M}^{-1} \text{ s}^{-1}$) [61,64]. As displayed in Fig. 9, the poor BA and NB degradation was obtained in all DSLBs/PMS systems. Noticeably, the reaction rate constant of BA with DSLB-800 catalyst reached 0.0043 min^{-1} , much higher than that with other catalysts. Furthermore, the lowest reaction rate constant of NB (0.0019 min^{-1}) was observed in DSLB-800/PMS system. Clearly, both $\bullet\text{OH}$ and $\text{SO}_4^{\bullet-}$ radicals participated in contaminants degradation. In comparison, fast degradation of FFA was achieved in DSLBs/PMS systems. Also, the k values of FFA degradation were higher than those of BA and NB removal. Besides, the k value of FFA increased markedly from 0.0080 to 0.1163 min^{-1} with pyrolysis temperature of DSLB rising from 500°C to 800°C . These results revealed the contribution of $\bullet\text{OH}$ and ${}^1\text{O}_2$ in DSLBs/PMS reactor, which were well consistent with the results of EPR analysis and quenching experiments.

The steady-state concentrations of $\bullet\text{OH}$, $\text{SO}_4^{\bullet-}$ and ${}^1\text{O}_2$ in the DSLBs/PMS systems could be calculated based on Eqs. S1–S8 (Text S7). As shown in Table S1, the steady-state concentration of ${}^1\text{O}_2$ in PMS system increased gradually with the DSLBs preparation temperature, which reached the highest ($1.53 \times 10^{-11} \text{ M}^{-1} \text{ s}^{-1}$) in DSLB-800/PMS system. Comparatively, the steady-state concentrations of ${}^1\text{O}_2$ were higher than those of $\text{SO}_4^{\bullet-}$ and $\bullet\text{OH}$ in DSLBs/PMS systems. Particularly, the steady-state concentration of ${}^1\text{O}_2$ in DSLB-800/PMS system was two and four orders of magnitude larger than that of $\text{SO}_4^{\bullet-}$ and $\bullet\text{OH}$. Thus, ${}^1\text{O}_2$ oxidation might be the dominant route for contaminants degradation in DSLBs/PMS systems.

3.4.3. Contributions of different active sites to ROSs generation

Currently, the contribution of individual active site to the oxidation system has been reported. A one-dimensional linear relationship between the organic compound degradation rate and the active site has been constructed. Actually, different active sites may interact with each other and work together to ROSs generation. Besides, different ROSs may react with each other, promoting contaminant degradation

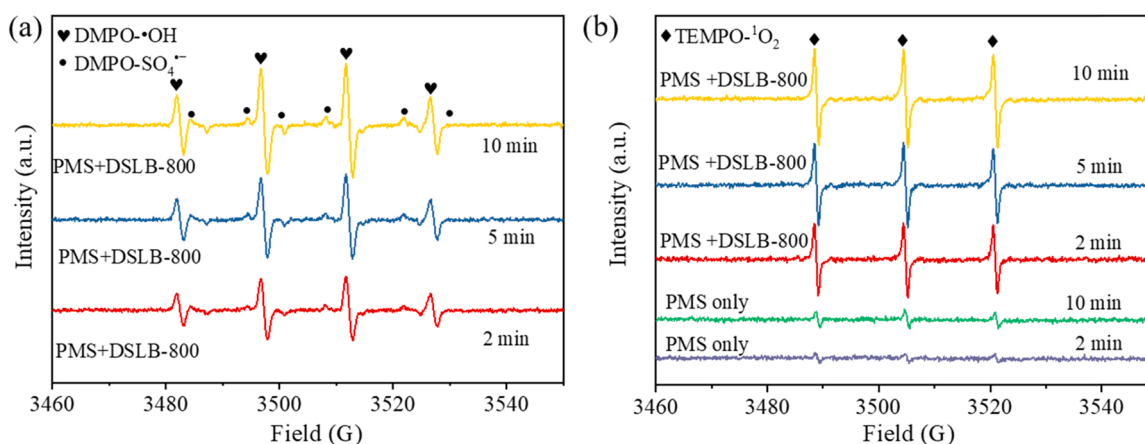


Fig. 8. EPR spectra of (a) $\bullet\text{OH}/\text{SO}_4^{\bullet-}$ and (b) ${}^1\text{O}_2$ in DSLB-800/PMS system. Reaction conditions: $[\text{DSL800}] = 2.0 \text{ g/L}$; $[\text{PMS}] = 2.5 \text{ mM}$; $[\text{SMX}]_0 = 15 \text{ mg/L}$; $\text{pH} = 5.24$; $T = 25^\circ\text{C}$; $[\text{DMPO}]_0 = 100 \text{ mM}$; $[\text{TEMP}]_0 = 10 \text{ mM}$.

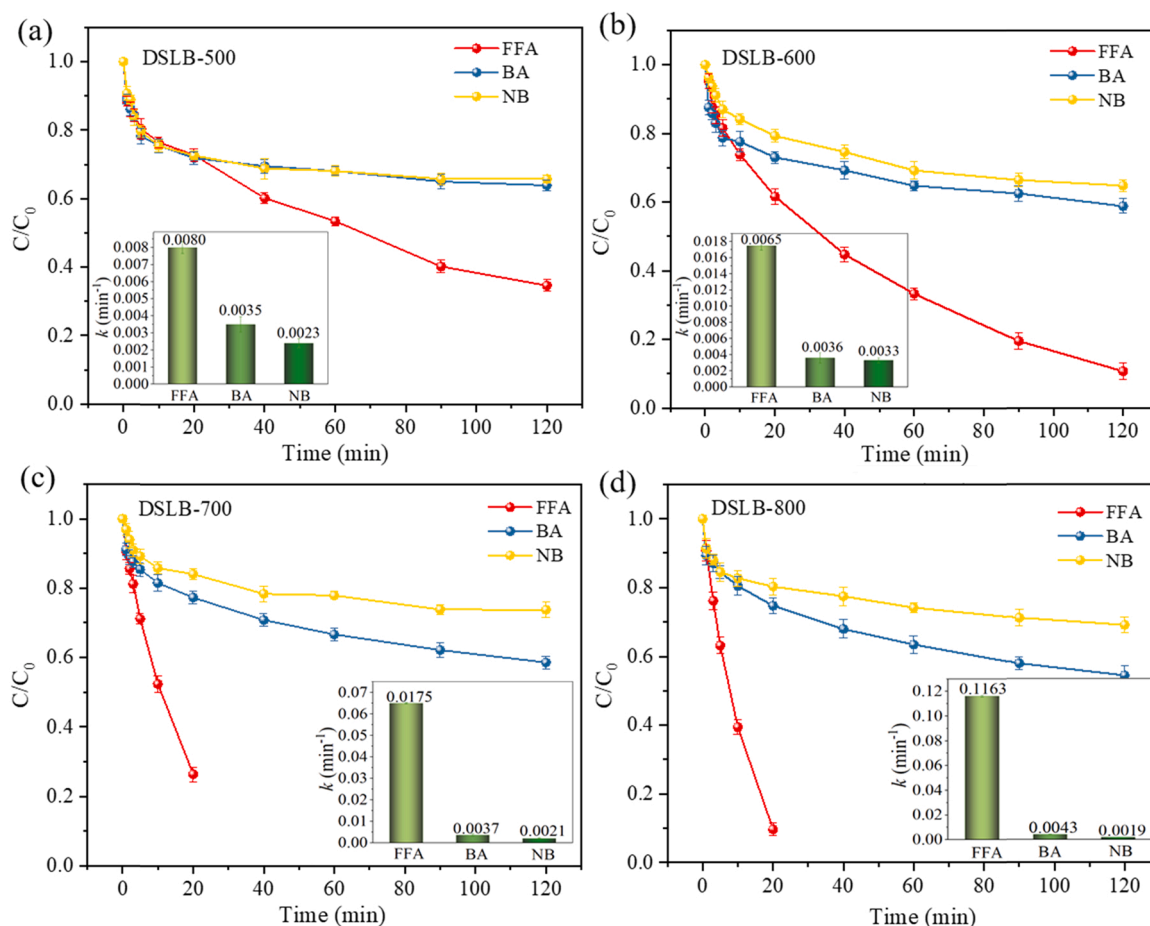


Fig. 9. Degradation of NB, BA and FFA in the DSLBs/PMS system (a) DSLB-500, (b) DSLB-600, (c) DSLB-700 and (d) DSLB-800 with corresponding kinetic rate constants inserted. Reaction conditions: [DSLBs] = 2.0 g/L; [PMS]₀ = 2.5 mM; pH = 5.24; T = 25 °C; [FFA]₀ = [NB]₀ = [BA]₀ = 0.01 mM.

synergistically. To further reveal the relationships between different active sites and ROSSs, multivariate equations were constructed between the total SMX degradation rate constants and the rate constants controlled by single ROS. Meanwhile, multivariate equations were also constructed between the degradation rate constants contributed by each ROS and the content of active sites.

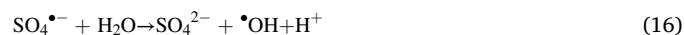
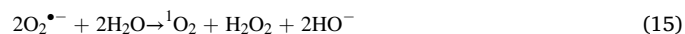
The relationship of the rate constant of each active specie and the total SMX degradation rate constant (k) was described in Eq. 10 with $R^2 = 0.966$. As regards the role of individual ROS, the positive factors of $\bullet\text{OH}$, $\text{SO}_4^{\bullet-}$ and $^1\text{O}_2$ in Eq. 10 indicated the acceleration of the k , enhancing SMX degradation. Considering the possible interactions among different species, the negative value of coupled $\bullet\text{OH}$ and $\text{SO}_4^{\bullet-}$ in Eq. 10 suggested little synergistic effect on the SMX degradation. A similar undermining effect was also observed for coupled $\text{SO}_4^{\bullet-}$ and $^1\text{O}_2$. The phenomenon might be attributed to the involved interconversion and reaction depletion among active species in the system. Specifically, the $\text{SO}_4^{\bullet-}$ generated from PMS activation could react with H_2O to produce $\bullet\text{OH}$ and SO_4^{2-} , in which $\text{SO}_4^{\bullet-}$ was consumed (Eq. 11) [65]. Under another scenario, $\text{SO}_4^{\bullet-}$ could react with H^+ in the presence of electrons, transforming to $\text{HSO}_4^{\bullet-}$ with weak oxidizing property (Eq. 12) [66]. Similar negative effect was also obtained by coupling $\bullet\text{OH}$ and $^1\text{O}_2$. The $\bullet\text{OH}$ could react with HSO_5^- , forming $\text{SO}_5^{\bullet-}$ with weak oxidizing property (Eq. 13) [67].

$$Y = 87.34X_1X_2X_3 - 6626.64X_1X_2 + 75.42X_1X_3 - 0.09X_2X_3 + 9.79 \times 10^9X_1 + 3.35 \times 10^9X_2 + 2.07 \times 10^7X_3 \quad (10)$$

where Y is the total rate constant of SMX degradation; X_1 , X_2 and X_3 are $[\bullet\text{OH}]_{\text{ss}}$, $[\text{SO}_4^{\bullet-}]_{\text{ss}}$ and $[^1\text{O}_2]_{\text{ss}}$, respectively.



Importantly, the combined effect of $\bullet\text{OH}$, $\text{SO}_4^{\bullet-}$ and $^1\text{O}_2$ might be beneficial for acceleration of the total oxidation rate with the positive factor in Eq. 10. Additionally, the involved non-radical ($^1\text{O}_2$) pathways in PMS oxidation system activated by biochar (BC)-based catalyst of were shown in Eqs. 14 and 15. In detail, dissolve oxygen in the solution could combine with electrons from BC donations to generate $\text{O}_2^{\bullet-}$ and then converted into $^1\text{O}_2$ [68]. Besides, the $\text{SO}_4^{\bullet-}$ reacted with H_2O to release $\bullet\text{OH}$ (Eq. 16). Afterwards, the $\bullet\text{OH}$ could transform to HO_2^{\bullet} and $\text{O}_2^{\bullet-}$ successively, which further turned into $^1\text{O}_2$ (Eqs. 15 and 17–19). Thus, the effects of reactive species were superimposed, promoting SMX degradation synergistically.



As the role of N-type sites of BC-based catalyst was significant for

PMS activation, the relationships of N-type sites and generated ROSs were analyzed and discussed. The roles of N-type active sites in ROSs generation were presented in Eqs. 20–22 with $R^2 > 0.998$. In terms of the role of individual active site, graphite N facilitated the generation of $\bullet\text{OH}$, $\text{SO}_4^{\bullet-}$ and $^1\text{O}_2$. Plenty of electrons could be attracted by the N sites from the adjacent C atoms. The electrons supplied by the electron-rich N group could induce the O-O bond breakage in PMS, producing $\bullet\text{OH}$ and $\text{SO}_4^{\bullet-}$ directly (Eqs. 23 and 24) [47,69]. Besides, the O-O bond in PMS as an electron donor could transfer electrons to the electron-deficient carbon atom, achieving PMS oxidation and $\text{SO}_5^{\bullet-}$ production. Subsequently, $^1\text{O}_2$ was generated via Eq. 25 [47,70].

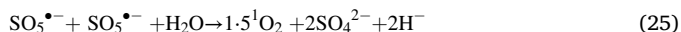
Different from the role of graphite N, pyridine N could make little contribution to the generation of $\bullet\text{OH}$, $\text{SO}_4^{\bullet-}$ and $^1\text{O}_2$. Comparatively, the adsorption energy of pyridine N to PMS was less than that of graphite N due to the weaker electronegativity, which imposed a lower effect on ROSs formation accordingly. However, pyrrole N alone might promote the generation of $\text{SO}_4^{\bullet-}$ and $^1\text{O}_2$ rather than $\bullet\text{OH}$. The O-H bond in PMS could be broken by pyrrole N with ultra-low energy barriers, producing $\text{SO}_5^{\bullet-}$ and H^+ (Eq. 26). In the same way, the $\bullet\text{OH}$ could transform to HO_2^{\bullet} and $\text{O}_2^{\bullet-}$ successively, which further turned into $^1\text{O}_2$ (Eqs. 15, 19 and 27). In consequence, $\bullet\text{OH}$ was consumed during participation in the $^1\text{O}_2$ generation.

$$Y_1 = 1.18X_1X_2X_3 + 0.32X_1X_2 + 0.039X_1X_3 + 0.75X_2X_3 + 0.01X_1 - 0.03X_2 - 0.005X_3 \quad (20)$$

$$Y_2 = 120.51X_1X_2X_3 + 6.65 \times 10^{-15}X_1X_2 - 0.55X_1X_3 - 2.27X_2X_3 + 2 \times 10^{-4}X_1 - 1.3 \times 10^{-3}X_2 + 0.01X_3 \quad (21)$$

$$Y_3 = 0.85X_1X_2X_3 + 0.98X_1X_2 + 0.18X_1X_3 + 2.31X_2X_3 + 0.03X_1 - 0.097X_2 + 0.017X_3 \quad (22)$$

Where Y_1 , Y_2 and Y_3 are the values of $[\bullet\text{OH}]_{ss}$, $[\text{SO}_4^{\bullet-}]_{ss}$ and $[^1\text{O}_2]_{ss}$; X_1 , X_2 and X_3 are the relative content of graphite N, pyridine N and pyrrole N, respectively.



Notably, the combined effect of pyridine N and pyrrole N, pyrrole N and graphite N might make little contribution to $\text{SO}_4^{\bullet-}$ generation. Due to the negative effect of pyridinic N alone, no synergistic effect between pyridine N and pyrrole N was observed for $\text{SO}_4^{\bullet-}$ generation. In comparison with other N-type sites, graphite N might induce high asymmetric spin and charge density of adjacent C atoms [71,72]. Thus, graphite N with higher electronegativity imposed a larger effect on ROS formation. However, the graphite N could be converted to pyrrole N with weaker electronegativity [13,69]. Therefore, no synergistic promotion was observed between graphite N and pyrrole N.

Based on positive factors of X_1X_3 in Eq. 20 and X_2X_3 in Eq. 22, the combination between graphite N and pyrrole N, pyridine N and pyrrole N might exhibit a synergistic effect on the formation of $\bullet\text{OH}$ and $^1\text{O}_2$. As reported, the thermal stability of pyrrole N and pyridine N was lower than that of graphite N [73]. Thus, the content of pyrrole N and pyridine N decreased while the graphite N content increased with pyrolysis temperature. Also, the graphite N exhibited a positive role in $\bullet\text{OH}$ and $^1\text{O}_2$ formation. As a result, the synergy between graphite N and pyrrole N, pyrrole N and pyridine N contributed to $\bullet\text{OH}$ and $^1\text{O}_2$ release. Similarly, positive factors of $X_1X_2X_3$ were also obtained in Eqs. 20–22. Clearly, the coupling effect of three N-type sites might contribute to the formation of $\bullet\text{OH}$, $\text{SO}_4^{\bullet-}$ and $^1\text{O}_2$.

Apart from N-type active sites, the relationships between O-

containing active sites and ROS generation were also investigated. The effect of O-containing active sites on the generation of ROSs was presented in Eqs. 28–30 with $R^2 > 0.995$. The formation of $\bullet\text{OH}$, $\text{SO}_4^{\bullet-}$ and $^1\text{O}_2$ were all promoted by single C=O, while C=O alone might promote the generation of $^1\text{O}_2$ rather than $\bullet\text{OH}$ and $\text{SO}_4^{\bullet-}$. The C atoms in C=O and C-O were capable of acquiring electrons from nearby O atoms owing to the electronegativity, promoting PMS activation and ROSs generation. Also, the generated $\bullet\text{OH}$ and $\text{SO}_4^{\bullet-}$ might be further converted into $\text{SO}_5^{\bullet-}$ by C=O via Eqs. 13 and 31. Thus, the $\bullet\text{OH}$ and $\text{SO}_4^{\bullet-}$ were consumed. Besides, the negative factor of X_2 in Eqs. 28–30 suggested the O=C-O sites might contribute little to $\bullet\text{OH}$, $\text{SO}_4^{\bullet-}$ and $^1\text{O}_2$ formation.

However, the combination of O=C-O and C-O lacked synergy for the generation of $\bullet\text{OH}$ and $\text{SO}_4^{\bullet-}$. Also, synergy of C=O, O=C-O and C-O could hardly facilitate the formation of $\text{SO}_4^{\bullet-}$ and $^1\text{O}_2$. The C-O sites were converted to C=O after PMS activation with less oxidizable $\text{SO}_5^{\bullet-}$ production [74] (Eq. 32). As mentioned, C=O site made little contribution to the production of $\bullet\text{OH}$ and $\text{SO}_4^{\bullet-}$ (Eqs. 28 and 29). Besides, the O=C-O site also lacked contribution to the production of $\text{SO}_4^{\bullet-}$ and $^1\text{O}_2$. Thus, little synergy was found between O=C-O and C-O, and among C=O, O=C-O and C-O for $\text{SO}_4^{\bullet-}$ and $^1\text{O}_2$ release.

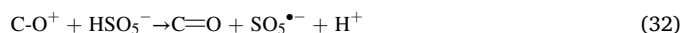
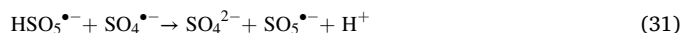
Notably, the combined effect of C=O and O=C-O promoted the generation of $\bullet\text{OH}$, $\text{SO}_4^{\bullet-}$ and $^1\text{O}_2$. The C=O sites could convert to C-O (Eq. 33), and C-O contributed to the generation of $\bullet\text{OH}$, $\text{SO}_4^{\bullet-}$ and $^1\text{O}_2$. Besides, O=C-O could act as an electron donor and facilitate the release of active species. Thus, the production of the three active species was enhanced by C=O and O=C-O cooperatively. Similarly, the combination of C=O, O=C-O and C-O might accelerate the generation of $\bullet\text{OH}$. Noticeably, a lone pair of electrons was held by the O atom in C=O, O=C-O and C-O. The three O-containing sites working together would enhance the generation of free radicals by coordinated electron transfer. The $\text{SO}_4^{\bullet-}$ could be further consumed, transforming to $\text{SO}_5^{\bullet-}$ with weak oxidizing property (Eq. 31).

$$Y_1 = 3.66 \times 10^{-9}X_1X_2X_3 + 2.35 \times 10^{-9}X_1X_2 - 1.52 \times 10^{-9}X_1X_3 - 2.66 \times 10^{-14}X_2X_3 - 8.18 \times 10^{-11}X_1 - 1.15 \times 10^{-10}X_2 + 1.09 \times 10^{-10}X_3 \quad (28)$$

$$Y_2 = -2.50 \times 10^{-7}X_1X_2X_3 + 1.99 \times 10^{-6}X_1X_2 - 2.39 \times 10^{-10}X_1X_3 - 4.89 \times 10^{-7}X_2X_3 - 1.17 \times 10^{-7}X_1 - 6.12 \times 10^{-8}X_2 + 6.98 \times 10^{-8}X_3 \quad (29)$$

$$Y_3 = -19.22X_1X_2X_3 + 6.33X_1X_2 - 10.55X_1X_3 + 7.30X_2X_3 + 0.17X_1 - 0.59X_2 + 0.23X_3 \quad (30)$$

where Y_1 , Y_2 and Y_3 are the values of $[\bullet\text{OH}]_{ss}$, $[\text{SO}_4^{\bullet-}]_{ss}$ and $[^1\text{O}_2]_{ss}$, respectively; X_1 , X_2 and X_3 are the relative contents of C=O, O=C-O and C-O, respectively.



In summary, the contributions of different active sites to ROSs were displayed in Fig. 10. Clearly, single graphite N and C-O contributed to the production of $\bullet\text{OH}$, $\text{SO}_4^{\bullet-}$ and $^1\text{O}_2$. The coupling effect between C=O and O=C=O, graphite N and pyridine N, graphite N and pyrrole N, pyridinic N and pyrrole N, as well as interactions among C=O, O=C=O and C-O, graphite N, pyridine N and pyrrole N were favorable for $\bullet\text{OH}$ generation. Besides, the separate pyrrole N, coupling effect between C=O and O=C=O, as well as the interactions among graphite N, pyridine N and pyrrole N exhibited positive effects on the release of $\text{SO}_4^{\bullet-}$. Furthermore, single pyrrole N, C=O and C-O, combined effect of C=O and O=C=O, O=C=O and C-O, graphite N and pyridine N, graphite N and pyrrole N, pyridine N and pyrrole N, as well as interactions among graphite N, pyridine N and pyrrole N contributed to $^1\text{O}_2$ release.

3.5. Contribution of defects to $^1\text{O}_2$ generation

According to quenching, EPR and chemical probe experiments, $^1\text{O}_2$

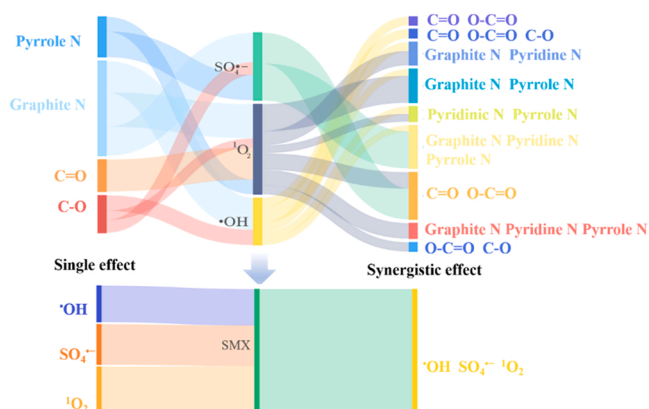


Fig. 10. The diagram of relationships between different sites and ROSs.

played key roles in SMX degradation. To identify the possible contribution of defects to $^1\text{O}_2$ formation, the correlation between $[\text{O}_2]_{\text{ss}}$ and I_D/I_G values was established. As shown in Fig. S7, a positive linear relationship with high correlation coefficient ($R^2 = 0.986$) was observed between I_D/I_G and $[\text{O}_2]_{\text{ss}}$ values. Obviously, defects were the intrinsic active centers on DSLBs for PMS activation and $^1\text{O}_2$ production.

As reported, four defects usually exist in carbon-based catalysts including single-vacancy (Defect I), double-vacancy (Defect II), added atomic (Defect III) and Stone-Wale defects (Defect IV) [46]. In order to further explore the dominant defect type in $^1\text{O}_2$ release, density functional theory (DFT) calculations of O-O bond length ($l_{\text{O-O}}$) and adsorption energy ($E_{\text{ads}} = E_{\text{carbon+PMS}} - E_{\text{carbon}} - E_{\text{PMS}}$) of PMS were performed.

The configurations of intact carbon and four defects were optimized and presented in Fig. 11 and Fig. S8. Furthermore, the $l_{\text{O-O}}$ and E_{ads} values of PMS on different carbon models were calculated. As displayed in Table S2. In comparison with $l_{\text{O-O}}$ value in free PMS (1.332 Å), the $l_{\text{O-O}}$ prolonged appreciably after PMS adsorption onto different carbon models, implying the occurrence of PMS activation at these carbon sites [47]. Noticeably, $l_{\text{O-O}}$ value of PMS adsorption on carbon models with defect II ($l_{\text{O-O}} = 1.452$ Å) was lower than those obtained with defect III ($l_{\text{O-O}} = 1.459$ Å), defect IV ($l_{\text{O-O}} = 1.469$ Å) and defect I ($l_{\text{O-O}} = 1.470$ Å). Similarly, among the four defect structures, the adsorption energy was the lowest after PMS adsorption on carbon models with defect II. These

results revealed that defect II site was the least favorable for preferential cleavage of O-O bonds in PMS to release $\bullet\text{OH}$ and $\text{SO}_4^{\bullet-}$ (radical pathway) for SMX degradation [75–77]. Instead, the defect II might prefer to cleave the O-H bond in PMS to produce $\text{SO}_5^{\bullet-}$ and thereby generate $^1\text{O}_2$ with H_2O (non-radical pathway) [78].

Besides, the charge density difference and the number of electron transfer between different carbon models and PMS were presented in Fig. 11f and g, and Fig. S9. Asymmetries were observed in the electron distribution on the surface of carbon models with four defect types compared to the intact carbon structure. The irregular distribution implied that the electrons at defects in DSLBs were more prone to participate in redox reactions [46]. Meanwhile, the defects in DSLBs exhibited a higher potential of electron transfer. Among them, the lowest electron transfer number between PMS and defect II ($Q = 0.792$ e) was noticed. Obviously, defect II in DSLBs was the preferential site for the breakage of O-H bond in PMS to produce $^1\text{O}_2$ [76]. These findings were well matched with the results of E_{ads} and $l_{\text{O-O}}$ analysis.

To further identify the activation pathway of defects for $^1\text{O}_2$ production, the adsorption energies between four types of defects and PMS molecules were calculated at different stages, as shown in Fig. 12. By comparing the negative values of exothermic reaction, the presence of each defect led to an easier activation of PMS than intact carbon model [79]. For the first reaction step, the reaction energy of defect II ($\Delta E = -2.2$ eV) on DSLB-800 surface with PMS adsorption was more negative than those of defect III ($\Delta E = -1.4$ eV), defect IV ($\Delta E = -0.8$ eV) and defect I ($\Delta E = -0.6$ eV). From the perspective of thermodynamic feasibility, these findings confirmed that defect II was more prone to the first reaction step. A similar phenomenon occurred in the second reaction step, while the third reaction process changed little. Usually, the first step is considered as a rate-determining step to generate $^1\text{O}_2$. Therefore, the double vacancy defect in DSLB-800 was determined as a preferential active site for PMS activation to produce $^1\text{O}_2$.

4. Conclusion

This work demonstrated a facile and efficient strategy for one-step synthesis of DSLBs with high content of graphite N, C=O and defect. As a result, the DSLB-800 exhibited better performance for SMX decomposition via PMS activation in a continuous fixed bed reactor. The dominant role of $^1\text{O}_2$ with the involvement of $\bullet\text{OH}$ and $\text{SO}_4^{\bullet-}$ were

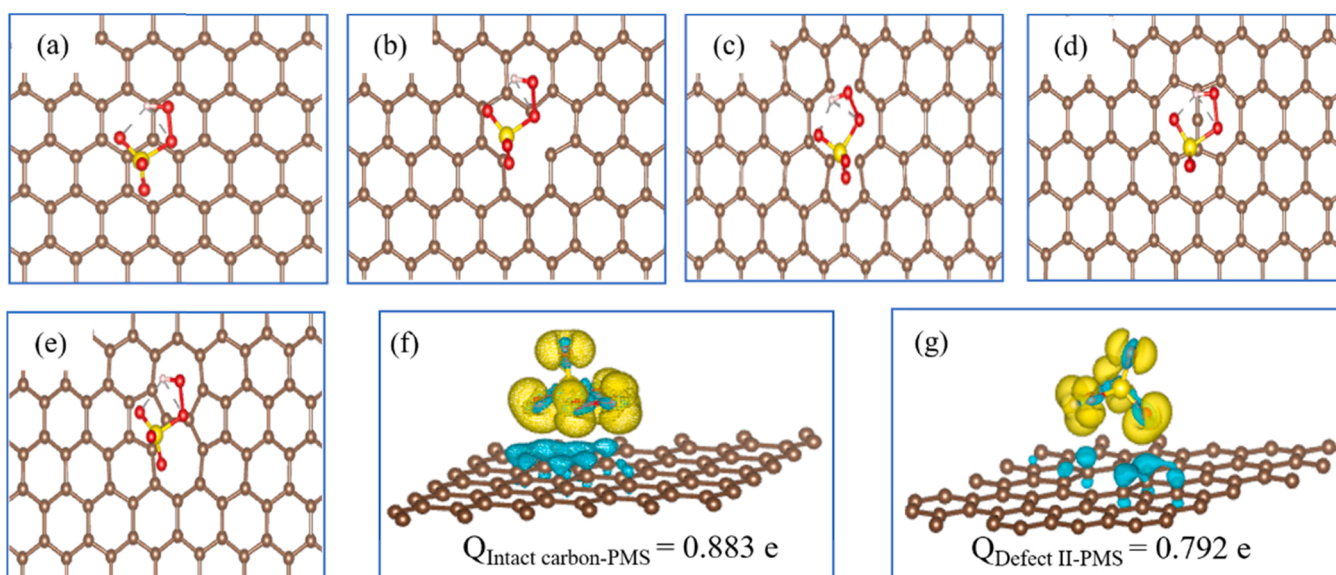


Fig. 11. Optimization configurations of (a) intact carbon, (b) single-vacancy defect, (c) double-vacancy defect, (d) add-atom defect, and (e) Stone-Wales defect; The charge density difference and the number of electron transfer between (f) intact carbon and PMS, (g) defect II and PMS (The yellow and blue represent the electron accumulation and deletion, respectively). (For interpretation of the references to color in this figure, the reader is referred to the web version of this article.)

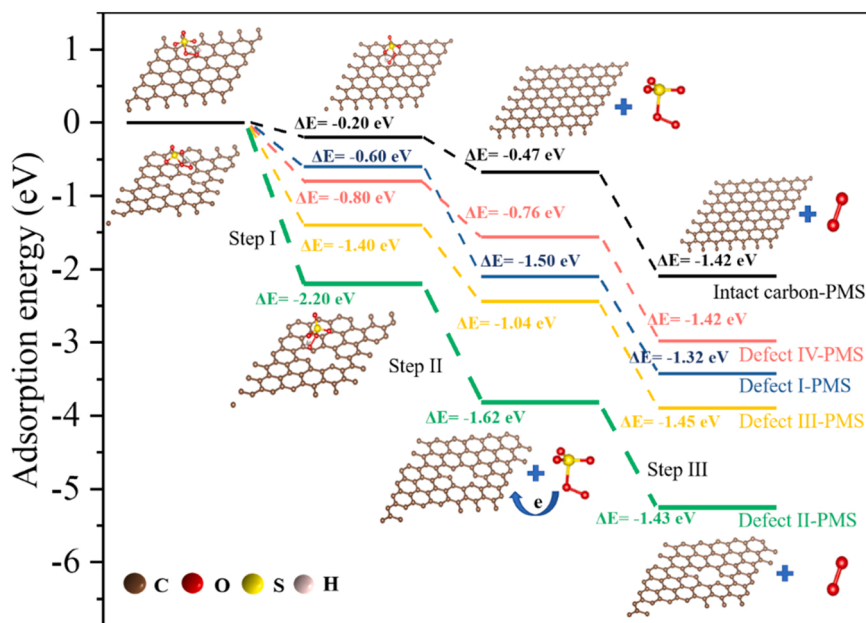


Fig. 12. Proposed mechanism of $^1\text{O}_2$ production via PMS activation with different types of defects in DSLBs.

revealed in SMX degradation system. Single defect, graphite N, C=O and C-O contributed to $^1\text{O}_2$ generation. Besides, the coupling effect between graphite N and pyridine N, graphite N and pyrrole N, pyridine N and pyrrole N, C=O and O=C-O, O=C-O and C-O, as well as among graphite N, pyridine N and pyrrole N were conducive to $^1\text{O}_2$ production. Furthermore, correlation analysis and DFT calculations confirmed the double vacancy defect in DSLB-800 was a preferential site for $^1\text{O}_2$ release among four types of defects. Benefiting from these unique mechanisms, the DSLBs loaded continuous flow fixed bed PMS reactor exhibited stability and durability, achieving efficient elimination of SMX from actual effluent. This study provides beneficial guidance for the resource utilization of DSL and offers theoretical support for the remediation of actual wastewater in continuous flow fixed bed PMS reactors.

CRediT authorship contribution statement

Yanshan Wang: Conceptualization, Methodology, Investigation, Validation, Writing – original draft, Writing – review & editing. **Wenzhao Peng:** Formal Analysis, Investigation, Writing – review & editing. **Jun Wang:** Calculation, Writing – review & editing. **Guanyi Chen:** Investigation, Writing – review & editing. **Ning Li:** Funding acquisition, Project administration, Supervision, Writing – review & editing. **Yingjin Song:** Project administration, Writing – review & editing. **Zhanjun Cheng:** Revision, Calculation, Writing – review & editing. **Beibei Yan:** Validation, Investigation. **Li'an Hou:** Supervision, Writing – review & editing. **Shaobin Wang:** Conceptualization, Writing – review & editing.

Declaration of Competing Interest

The authors declare that they have no known competing financial interests or personal relationships that could have appeared to influence the work reported in this paper.

Acknowledgments

This work was supported by the National Natural Science Foundation of China (52100156) and Shenzhen Science and Technology Program (GJHZ20200731095801005 and JCYJ20200109150210400).

Appendix A. Supporting information

Supplementary data associated with this article can be found in the online version at [doi:10.1016/j.apcatb.2022.121342](https://doi.org/10.1016/j.apcatb.2022.121342).

References

- [1] H.-B. Qiu, P.-C. Guo, L. Yuan, G.-P. Sheng, Different non-radical oxidation processes of persulfate and peroxymonosulfate activation by nitrogen-doped mesoporous carbon, *Chin. Chem. Lett.* 31 (2020) 2614–2618, <https://doi.org/10.1016/j.ccl.2020.08.014>.
- [2] G. Chen, L.-C. Nengzi, Y. Gao, G. Zhu, J. Gou, X. Cheng, Degradation of tartrazine by peroxymonosulfate through magnetic $\text{Fe}_2\text{O}_3/\text{Mn}_2\text{O}_3$ composites activation, *Chin. Chem. Lett.* 31 (2020) 2730–2736, <https://doi.org/10.1016/j.ccl.2020.02.033>.
- [3] Y. Wang, Y. Song, N. Li, W. Liu, B. Yan, Y. Yu, L. Liang, G. Chen, La Hou, S. Wang, Tunable active sites on biogas digestate derived biochar for sulfanilamide degradation by peroxymonosulfate activation, *J. Hazard. Mater.* 421 (2022), 126794, <https://doi.org/10.1016/j.jhazmat.2021.126794>.
- [4] P. Ding, J. Niu, F. Chang, Z. He, T. Wågberg, Z. Li, G. Hu, NiCo2O4 hollow microsphere-mediated ultrafast peroxymonosulfate activation for dye degradation, *Chin. Chem. Lett.* 32 (2021) 2495–2498, <https://doi.org/10.1016/j.ccl.2020.12.063>.
- [5] Y. Peng, W. Tong, Y. Xie, W. Hu, Y. Li, Y. Zhang, Y. Wang, Yeast biomass-induced Co_2P /biochar composite for sulfonamide antibiotics degradation through peroxymonosulfate activation, *Environ. Pollut.* 268 (2021), 115930, <https://doi.org/10.1016/j.envpol.2020.115930>.
- [6] Y. Yu, N. Li, X. Lu, B. Yan, G. Chen, Y. Wang, X. Duan, Z. Cheng, S. Wang, Co/N co-doped carbonized wood sponge with 3D porous framework for efficient peroxymonosulfate activation: performance and internal mechanism, *J. Hazard. Mater.* 421 (2021), 126735, <https://doi.org/10.1016/j.jhazmat.2021.126735>.
- [7] S. Xiao, M. Cheng, H. Zhong, Z. Liu, Y. Liu, X. Yang, Q. Liang, Iron-mediated activation of persulfate and peroxymonosulfate in both homogeneous and heterogeneous ways: a review, *Chem. Eng. J.* 384 (2020), 123265, <https://doi.org/10.1016/j.cej.2019.123265>.
- [8] Y. Hong, J. Peng, X. Zhao, Y. Yan, B. Lai, G. Yao, Efficient degradation of atrazine by CoMgAl layered double oxides catalyzed peroxymonosulfate: optimization, degradation pathways and mechanism, *Chem. Eng. J.* 370 (2019) 354–363, <https://doi.org/10.1016/j.cej.2019.03.127>.
- [9] Y.-Y. Ahn, H. Bae, H.-I. Kim, S.-H. Kim, J.-H. Kim, S.-G. Lee, J. Lee, Surface-loaded metal nanoparticles for peroxymonosulfate activation: efficiency and mechanism reconnaissance, *Appl. Catal. B: Environ.* 241 (2019) 561–569, <https://doi.org/10.1016/j.apcatb.2018.09.056>.
- [10] Q. Qin, T. Liu, J. Zhang, R. Wei, S. You, Y. Xu, Facile synthesis of oxygen vacancies enriched $\alpha\text{-Fe}_2\text{O}_3$ for peroxymonosulfate activation: a non-radical process for sulfamethoxazole degradation, *J. Hazard. Mater.* 419 (2021), 126447, <https://doi.org/10.1016/j.jhazmat.2021.126447>.
- [11] T.D. Minh, M.C. Ncibi, V. Srivastava, S.K. Thangaraj, J. Jäms, M. Sillanpää, Gingerbread ingredient-derived carbons-assembled CNT foam for the efficient peroxymonosulfate-mediated degradation of emerging pharmaceutical

- contaminants, *Appl. Catal. B Environ.* 244 (2019) 367–384, <https://doi.org/10.1016/j.apcatb.2018.11.064>.
- [12] Y. Gao, Y. Zhu, L. Lyu, Q. Zeng, X. Xing, C. Hu, Electronic structure modulation of graphitic carbon nitride by oxygen oping for enhanced catalytic degradation of organic pollutants through peroxymonosulfate activation, *Environ. Sci. Technol.* 52 (2018) 14371–14380, <https://doi.org/10.1021/acs.est.8b05246>.
- [13] X. Chen, W.-D. Oh, Z.-T. Hu, Y.-M. Sun, R.D. Webster, S.-Z. Li, T.-T. Lim, Enhancing sulfacetamide degradation by peroxymonosulfate activation with N-doped graphene produced through delicately-controlled nitrogen functionalization via tweaking thermal annealing processes, *Appl. Catal. B Environ.* 225 (2018) 243–257, <https://doi.org/10.1016/j.apcatb.2017.11.071>.
- [14] M.B. Ahmed, J.L. Zhou, H.H. Ngo, W. Guo, M.A.H. Johir, K. Sornalingam, Single and competitive sorption properties and mechanism of functionalized biochar for removing sulfonamide antibiotics from water, *Chem. Eng. J.* 311 (2017) 348–358, <https://doi.org/10.1016/j.cej.2016.11.106>.
- [15] Y.D. Chen, R. Wang, X. Duan, S. Wang, N.Q. Ren, S.H. Ho, Production, properties, and catalytic applications of sludge derived biochar for environmental remediation, *Water Res.* 187 (2020), 116390, <https://doi.org/10.1016/j.watres.2020.116390>.
- [16] T. Do Minh, J. Song, A. Deb, L. Cha, V. Srivastava, M. Sillanpää, Biochar based catalysts for the abatement of emerging pollutants: a review, *Chem. Eng. J.* 394 (2020), 124856, <https://doi.org/10.1016/j.cej.2020.124856>.
- [17] C. Zhao, B. Shao, M. Yan, Z. Liu, Q. Liang, Q. He, T. Wu, Y. Liu, Y. Pan, J. Huang, J. Wang, J. Liang, L. Tang, Activation of peroxymonosulfate by biochar-based catalysts and applications in the degradation of organic contaminants: a review, *Chem. Eng. J.* 416 (2021), 128829, <https://doi.org/10.1016/j.cej.2021.128829>.
- [18] P. Duan, Y. Qi, S. Feng, X. Peng, W. Wang, Y. Yue, Y. Shang, Y. Li, B. Gao, X. Xu, Enhanced degradation of clothianidin in peroxymonosulfate/catalyst system via core-shell FeMn @ N-C and phosphate surrounding, *Appl. Catal. B Environ.* 267 (2020), 118717, <https://doi.org/10.1016/j.apcatb.2020.118717>.
- [19] L. Jin, S. You, X. Duan, Y. Yao, J. Yang, Y. Liu, Peroxymonosulfate activation by Fe₃O₄-MnO₂/CNT nanohybrid electroactive filter towards ultrafast micropollutants decontamination: performance and mechanism, *J. Hazard. Mater.* 423 (2022), 127111, <https://doi.org/10.1016/j.jhazmat.2021.127111>.
- [20] J. Yu, H. Feng, L. Tang, Y. Pang, G. Zeng, Y. Lu, H. Dong, J. Wang, Y. Liu, C. Feng, J. Wang, B. Peng, S. Ye, Metal-free carbon materials for persulfate-based advanced oxidation process: microstructure, property and tailoring, *Prog. Mater. Sci.* 111 (2020), 100654, <https://doi.org/10.1016/j.pmatsci.2020.100654>.
- [21] M. Zhang, G. Song, D.L. Gelardi, L. Huang, E. Khan, O. Masek, S.J. Parikh, Y.S. Ok, Evaluating biochar and its modifications for the removal of ammonium, nitrate, and phosphate in water, *Water Res.* 186 (2020), 116303, <https://doi.org/10.1016/j.watres.2020.116303>.
- [22] K. Li, S. Ma, S. Xu, H. Fu, Z. Li, Y. Li, S. Liu, J. Du, The mechanism changes during bisphenol A degradation in three iron functionalized biochar/peroxymonosulfate systems: The crucial roles of iron contents and graphitized carbon layers, *J. Hazard. Mater.* 404 (2021), 124145, <https://doi.org/10.1016/j.jhazmat.2020.124145>.
- [23] Y. Hu, D. Chen, R. Zhang, Y. Ding, Z. Ren, M. Fu, X. Cao, G. Zeng, Singlet oxygen-dominated activation of peroxymonosulfate by passion fruit shell derived biochar for catalytic degradation of tetracycline through a non-radical oxidation pathway, *J. Hazard. Mater.* 419 (2021), 126495, <https://doi.org/10.1016/j.jhazmat.2021.126495>.
- [24] R. Zhang, Y. Li, Z. Wang, Y. Tong, P. Sun, Biochar-activated peroxydisulfate as an effective process to eliminate pharmaceutical and metabolite in hydrolyzed urine, *Water Res.* 177 (2020), 115809, <https://doi.org/10.1016/j.watres.2020.115809>.
- [25] C.M. Hung, C.P. Huang, C.W. Chen, C.D. Dong, Degradation of organic contaminants in marine sediments by peroxymonosulfate over LaFeO₃ nanoparticles supported on water caltrop shell-derived biochar and the associated microbial community responses, *J. Hazard. Mater.* 420 (2021), 126553, <https://doi.org/10.1016/j.jhazmat.2021.126553>.
- [26] A. Jawad, K. Zhan, H. Wang, A. Shahzad, Z. Zeng, J. Wang, X. Zhou, H. Ullah, Z. Chen, Z. Chen, Tuning of persulfate activation from a free radical to a nonradical pathway through the incorporation of non-redox magnesium oxide, *Environ. Sci. Technol.* 54 (2020) 2476–2488, <https://doi.org/10.1021/acs.est.9b04696>.
- [27] R. Yin, W. Guo, H. Wang, J. Du, Q. Wu, J.-S. Chang, N. Ren, Singlet oxygen-dominated peroxydisulfate activation by sludge-derived biochar for sulfamethoxazole degradation through a nonradical oxidation pathway: performance and mechanism, *Chem. Eng. J.* 357 (2019) 589–599, <https://doi.org/10.1016/j.cej.2018.09.184>.
- [28] (a) (doi) S. Wang, J. Wang, Peroxymonosulfate activation by Co9S8@S and N co-doped biochar for sulfamethoxazole degradation, *Chem. Eng. J.* 385 (2020), 123933; (b) <https://doi.org/10.1016/j.cej.2018.09.184>, <https://doi.org/10.1016/j.cej.2019.123933> R. Yin, W. Guo, H. Wang, J. Du, Q. Wu, J.-S. Chang, N. Ren, Singlet oxygen-dominated peroxydisulfate activation by sludge-derived biochar for sulfamethoxazole degradation through a nonradical oxidation pathway: performance and mechanism, *Chem. Eng. J.* 357 (2019) 589–599.
- [29] D. Gao, M. Junaed, F. Lin, S. Zhang, N. Xu, Degradation of sulphachloropyridazine sodium in column reactor packed with CoFe₂O₄-loaded quartz sand via peroxymonosulfate activation: insights into the amorphous phase, efficiency, and mechanism, *Chem. Eng. J.* 390 (2020), 124549, <https://doi.org/10.1016/j.cej.2020.124549>.
- [30] Y. Jiang, R. Wang, Z. Yin, J. Sun, B. Wang, D. Zhao, X.A. Zeng, H. Li, M. Huang, B. Sun, Optimization of Jiuzao protein hydrolysis conditions and antioxidant activity in vivo of Jiuzao tetrapeptide Asp-Arg-Glu-Leu by elevating the Nrf2/Keap1-p38/PI3K-MafK signaling pathway, *Food Funct.* 12 (2021) 4808–4824, <https://doi.org/10.1039/D0FO02852E>.
- [31] W.-D. Oh, G. Lisak, R.D. Webster, Y.-N. Liang, A. Veksha, A. Giannis, J.G.S. Moo, J.-W. Lim, T.-T. Lim, Insights into the thermolytic transformation of lignocellulosic biomass waste to redox-active carbocatalyst: durability of surface active sites, *Appl. Catal. B Environ.* 233 (2018) 120–129, <https://doi.org/10.1016/j.apcatb.2018.03.106>.
- [32] S. Ye, G. Zeng, X. Tan, H. Wu, J. Liang, B. Song, N. Tang, P. Zhang, Y. Yang, Q. Chen, X. Li, Nitrogen-doped biochar fiber with graphitization from Boehmeria nivea for promoted peroxymonosulfate activation and non-radical degradation pathways with enhancing electron transfer, *Appl. Catal. B Environ.* 269 (2020), 118850, <https://doi.org/10.1016/j.apcatb.2020.118850>.
- [33] S.H. Ho, Y.D. Chen, R. Li, C. Zhang, Y. Ge, G. Cao, M. Ma, X. Duan, S. Wang, N. Q. Ren, N-doped graphitic biochars from C-phycocyanin extracted Spirulina residue for catalytic persulfate activation toward nonradical disinfection and organic oxidation, *Water Res.* 159 (2019) 77–86, <https://doi.org/10.1016/j.watres.2019.05.008>.
- [34] Z. Zhang, X. Huang, J. Ma, Z. Pei, L. Luo, X. Ke, F. Qin, Y. Li, R. Yang, Y. Zhu, Q. Zhang, Efficient removal of bisphenol S by non-radical activation of peroxydisulfate in the presence of nano-graphite, *Water Res.* 201 (2021), 117288, <https://doi.org/10.1016/j.watres.2021.117288>.
- [35] H. Wang, W. Guo, B. Liu, Q. Wu, H. Luo, Q. Zhao, Q. Si, F. Sseguya, N. Ren, Edge-nitrogenated biochar for efficient peroxydisulfate activation: an electron transfer mechanism, *Water Res.* 160 (2019) 405–414, <https://doi.org/10.1016/j.watres.2019.05.059>.
- [36] R. Guan, X. Li, A.C. Wachemo, H. Yuan, Y. Liu, D. Zou, X. Zuo, J. Gu, Enhancing anaerobic digestion performance and degradation of lignocellulosic components of rice straw by combined biological and chemical pretreatment, *Sci. Total Environ.*, 637–638 (2018) 9–17, <https://doi.org/10.1016/j.scitotenv.2018.04.366>.
- [37] X. Dai, Y. Hua, R. Liu, S. Chen, H. Li, L. Dai, C. Cai, Biomethane production by typical straw anaerobic digestion: deep insights of material compositions and surface properties, *Bioresour. Technol.* 313 (2020), 123643, <https://doi.org/10.1016/j.biortech.2020.123643>.
- [38] M.M. Mian, G. Liu, B. Fu, Y. Song, Facile synthesis of sludge-derived MnOx-N-biochar as an efficient catalyst for peroxymonosulfate activation, *Appl. Catal. B Environ.* 255 (2019), 117765, <https://doi.org/10.1016/j.apcatb.2019.117765>.
- [39] L. Du, W. Xu, S. Liu, X. Li, D. Huang, X. Tan, Y. Liu, Activation of persulfate by graphitized biochar for sulfamethoxazole removal: the roles of graphitic carbon structure and carbonyl group, *J. Colloid Interface Sci.* 577 (2020) 419–430, <https://doi.org/10.1016/j.jcis.2020.05.096>.
- [40] D. Huang, Q. Zhang, C. Zhang, R. Wang, R. Deng, H. Luo, T. Li, J. Li, S. Chen, C. Liu, Mn doped magnetic biochar as persulfate activator for the degradation of tetracycline, *Chem. Eng. J.* 391 (2020), 123532, <https://doi.org/10.1016/j.cej.2019.123532>.
- [41] D. Kim, K. Lee, K.Y. Park, Upgrading the characteristics of biochar from cellulose, lignin, and xylan for solid biofuel production from biomass by hydrothermal carbonization, *J. Ind. Eng. Chem.* 42 (2016) 95–100, <https://doi.org/10.1016/j.jiec.2016.07.037>.
- [42] S. Xin, B. Ma, C. Zhang, X. Ma, P. Xu, G. Zhang, M. Gao, Y. Xin, Catalytic activation of peroxydisulfate by alfalfa-derived nitrogen self-doped porous carbon supported CuFe₂O₄ for nimesulide degradation: performance, mechanism and DFT calculation, *Appl. Catal. B Environ.* 294 (2021), 120247, <https://doi.org/10.1016/j.apcatb.2021.120247>.
- [43] Y. Wang, Y. Li, Y. Zhang, Y. Song, B. Yan, W. Wu, L. Zhong, N. Li, G. Chen, L. Hou, Hydrothermal carbonization of garden waste by pretreatment with anaerobic digestion to improve hydrochar performance and energy recovery, *Sci. Total Environ.* (2021), 151014, <https://doi.org/10.1016/j.scitotenv.2021.151014>.
- [44] S. Wang, L. Xu, J. Wang, Nitrogen-doped graphene as peroxymonosulfate activator and electron transfer mediator for the enhanced degradation of sulfamethoxazole, *Chem. Eng. J.* 375 (2019), 122041, <https://doi.org/10.1016/j.cej.2019.122041>.
- [45] L. Liang, G. Chen, N. Li, H. Liu, B. Yan, Y. Wang, X. Duan, L. Hou, S. Wang, Active sites decoration on sewage sludge-red mud complex biochar for persulfate activation to degrade sulfanilamide, *J. Colloid Interface Sci.* (2021) 1983–1998, <https://doi.org/10.1016/j.jcis.2021.10.150>.
- [46] P. Shao, S. Yu, X. Duan, L. Yang, H. Shi, L. Ding, J. Tian, L. Yang, X. Luo, S. Wang, Potential difference driving electron transfer via defective carbon nanotubes toward selective oxidation of organic micropollutants, *Environ. Sci. Technol.* 54 (2020) 8464–8472, <https://doi.org/10.1021/acs.est.0c02645>.
- [47] Y. Gao, Z. Chen, Y. Zhu, T. Li, C. Hu, New insights into the generation of singlet oxygen in the metal-free peroxymonosulfate activation process: important role of electron-deficient carbon atoms, *Environ. Sci. Technol.* 54 (2020) 1232–1241, <https://doi.org/10.1021/acs.est.9b05856>.
- [48] B. Liu, W. Guo, H. Wang, Q. Si, Q. Zhao, H. Luo, N. Ren, B-doped graphitic porous biochar with enhanced surface affinity and electron transfer for efficient peroxydisulfate activation, *Chem. Eng. J.* 396 (2020), 125119, <https://doi.org/10.1016/j.cej.2020.125119>.
- [49] S. Cai, Q. Zhang, Z. Wang, S. Hua, D. Ding, T. Cai, R. Zhang, Pyrrolic N-rich biochar without exogenous nitrogen doping as a functional material for bisphenol A removal: performance and mechanism, *Appl. Catal. B Environ.* 291 (2021), 120093, <https://doi.org/10.1016/j.apcatb.2021.120093>.
- [50] M. Xi, K. Cui, M. Cui, Y. Ding, Z. Guo, Y. Chen, C. Li, X. Li, Enhanced norfloxacin degradation by iron and nitrogen co-doped biochar: revealing the radical and nonradical co-dominant mechanism of persulfate activation, *Chem. Eng. J.* 420 (2021), 129902, <https://doi.org/10.1016/j.cej.2021.129902>.
- [51] L. Tang, Y. Liu, J. Wang, G. Zeng, Y. Deng, H. Dong, H. Feng, J. Wang, B. Peng, Enhanced activation process of persulfate by mesoporous carbon for degradation of aqueous organic pollutants: electron transfer mechanism, *Appl. Catal. B Environ.* 231 (2018) 1–10, <https://doi.org/10.1016/j.apcatb.2018.02.059>.

- [52] M. Teixeira, J.J. Pignatello, J.L. Beltran, M. Granados, J. Peccia, Speciation of the ionizable antibiotic sulfamethazine on black carbon (biochar), *Environ. Sci. Technol.* 45 (2011) 10020–10027, <https://doi.org/10.1021/es202487h>.
- [53] P. Hu, M. Long, Cobalt-catalyzed sulfate radical-based advanced oxidation: a review on heterogeneous catalysts and applications, *Appl. Catal. B: Environ.* 181 (2016) 103–117, <https://doi.org/10.1016/j.apcatb.2015.07.024>.
- [54] J. Wang, S. Wang, Effect of inorganic anions on the performance of advanced oxidation processes for degradation of organic contaminants, *Chem. Eng. J.* 411 (2021), 128392, <https://doi.org/10.1016/j.cej.2020.128392>.
- [55] X. Wu, X. Gu, S. Lu, Z. Qiu, Q. Sui, X. Zang, Z. Miao, M. Xu, Strong enhancement of trichloroethylene degradation in ferrous ion activated persulfate system by promoting ferric and ferrous ion cycles with hydroxylamine, *Sep. Puri. Technol.* 147 (2015) 186–193, <https://doi.org/10.1016/j.seppur.2015.04.031>.
- [56] X. Li, Y. Jia, M. Zhou, X. Su, J. Sun, High-efficiency degradation of organic pollutants with Fe, N co-doped biochar catalysts via persulfate activation, *J. Hazard. Mater.* 397 (2020), 122764, <https://doi.org/10.1016/j.jhazmat.2020.122764>.
- [57] W.L. Wang, Q.Y. Wu, N. Huang, T. Wang, H.Y. Hu, Synergistic effect between UV and chlorine (UV/chlorine) on the degradation of carbamazepine: influence factors and radical species, *Water Res.* 98 (2016) 190–198, <https://doi.org/10.1016/j.watres.2016.04.015>.
- [58] J. Peng, X. Lu, X. Jiang, Y. Zhang, Q. Chen, B. Lai, G. Yao, Degradation of atrazine by persulfate activation with copper sulfide (CuS): kinetics study, degradation pathways and mechanism, *Chem. Eng. J.* 354 (2018) 740–752, <https://doi.org/10.1016/j.cej.2018.08.038>.
- [59] J. Wang, S. Wang, Activation of persulfate (PS) and peroxymonosulfate (PMS) and application for the degradation of emerging contaminants, *Chem. Eng. J.* 334 (2018) 1502–1517, <https://doi.org/10.1016/j.cej.2017.11.059>.
- [60] X. Zhou, C. Luo, M. Luo, Q. Wang, J. Wang, Z. Liao, Z. Chen, Z. Chen, Understanding the synergetic effect from foreign metals in bimetallic oxides for PMS activation: A common strategy to increase the stoichiometric efficiency of oxidants, *Chem. Eng. J.* 381 (2020), 122587, <https://doi.org/10.1016/j.cej.2019.122587>.
- [61] S. Zhu, X. Li, J. Kang, X. Duan, S. Wang, Persulfate activation on crystallographic manganese oxides: mechanism of singlet oxygen evolution for nonradical selective degradation of aqueous contaminants, *Environ. Sci. Technol.* 53 (2019) 307–315, <https://doi.org/10.1021/acs.est.8b04669>.
- [62] H. Dong, Y. Li, S. Wang, W. Liu, G. Zhou, Y. Xie, X. Guan, Both Fe(IV) and radicals are active oxidants in the Fe(II)/peroxydisulfate process, *Environ. Sci. Technol. Lett.* 7 (2020) 219–224, <https://doi.org/10.1021/acs.estlett.0c00025>.
- [63] B. Huang, Z. Xiong, P. Zhou, H. Zhang, Z. Pan, G. Yao, B. Lai, Ultrafast degradation of contaminants in a trace cobalt(II) activated peroxymonosulfate process triggered through borate: indispensable role of intermediate complex, *J. Hazard. Mater.* 424 (2022), 127641, <https://doi.org/10.1016/j.jhazmat.2021.127641>.
- [64] D. He, H. Yang, D. Jin, J. Qu, X. Yuan, Y.-n Zhang, M. Huo, W.J. G.M. Peijnenburg, Rapid water purification using modified graphitic carbon nitride and visible light, *Appl. Catal. B: Environ.* 285 (2021), 119864, <https://doi.org/10.1016/j.apcatb.2020.119864>.
- [65] Q. Wang, Z. Xu, Y. Cao, Y. Chen, X. Du, Y. Yang, Z. Wang, Two-dimensional ultrathin perforated Co₃O₄ nanosheets enhanced PMS-activated selective oxidation of organic micropollutants in environmental remediation, *Chem. Eng. J.* 427 (2022), 131953, <https://doi.org/10.1016/j.cej.2021.131953>.
- [66] S. Zhu, Y. Xu, Z. Zhu, Z. Liu, W. Wang, Activation of peroxymonosulfate by magnetic Co-Fe/SiO₂ layered catalyst derived from iron sludge for ciprofloxacin degradation, *Chem. Eng. J.* 384 (2020), 123298, <https://doi.org/10.1016/j.cej.2019.123298>.
- [67] D. Ouyang, Y. Chen, J. Yan, L. Qian, L. Han, M. Chen, Activation mechanism of peroxymonosulfate by biochar for catalytic degradation of 1,4-dioxane: important role of biochar defect structures, *Chem. Eng. J.* 370 (2019) 614–624, <https://doi.org/10.1016/j.cej.2019.03.235>.
- [68] S. Huang, T. Wang, K. Chen, M. Mei, J. Liu, J. Li, Engineered biochar derived from food waste digestate for activation of peroxymonosulfate to remove organic pollutants, *Waste Manag.* 107 (2020) 211–218, <https://doi.org/10.1016/j.wasman.2020.04.009>.
- [69] S. Liu, Z. Zhang, F. Huang, Y. Liu, L. Feng, J. Jiang, L. Zhang, F. Qi, C. Liu, Carbonized polyaniline activated peroxymonosulfate (PMS) for phenol degradation: role of PMS adsorption and singlet oxygen generation, *Appl. Catal. B: Environ.* 286 (2021), 119921, <https://doi.org/10.1016/j.apcatb.2021.119921>.
- [70] S. Wang, Y. Liu, J. Wang, Peroxymonosulfate Activation by Fe-Co-O-Codoped graphite carbon nitride for degradation of sulfamethoxazole, *Environ. Sci. Technol.* 54 (2020) 10361–10369, <https://doi.org/10.1021/acs.est.0c03256>.
- [71] J. Wang, X. Duan, J. Gao, Y. Shen, X. Feng, Z. Yu, X. Tan, S. Liu, S. Wang, Roles of structure defect, oxygen groups and heteroatom doping on carbon in nonradical oxidation of water contaminants, *Water Res.* 185 (2020), 116244, <https://doi.org/10.1016/j.watres.2020.116244>.
- [72] X. Duan, H. Sun, Y. Wang, J. Kang, S. Wang, N-doping-induced nonradical reaction on single-walled carbon nanotubes for catalytic phenol oxidation, *ACS Catal.* 5 (2014) 553–559, <https://doi.org/10.1021/cs5017613>.
- [73] J. Miao, W. Geng, P.J.J. Alvarez, M. Long, 2D N-doped porous carbon derived from polydopamine-coated graphitic carbon nitride for efficient nonradical activation of peroxymonosulfate, *Environ. Sci. Technol.* 54 (2020) 8473–8481, <https://doi.org/10.1021/acs.est.0c03207>.
- [74] M. Kohantorabi, G. Moussavi, S. Giannakis, A review of the innovations in metal- and carbon-based catalysts explored for heterogeneous peroxymonosulfate (PMS) activation, with focus on radical vs. non-radical degradation pathways of organic contaminants, *Chem. Eng. J.* 411 (2021), 127957, <https://doi.org/10.1016/j.cej.2020.127957>.
- [75] R. Wang, X. Zhang, L. Zhao, J. Feng, T. Wei, Y. Ren, Y. Shen, In-situ synthesis of Fe and O co-doped g-C₃N₄ to enhance peroxymonosulfate activation with favorable charge transfer for efficient contaminant decomposition, *J. Taiwan Inst. Chem. E.* 115 (2020) 198–207, <https://doi.org/10.1016/j.jtice.2020.10.022>.
- [76] J. Wei, D. Han, J. Bi, J. Gong, Fe-doped ilmenite CoTiO₃ for antibiotic removal: electronic modulation and enhanced activation of peroxymonosulfate, *Chem. Eng. J.* 423 (2021), 130165, <https://doi.org/10.1016/j.cej.2021.130165>.
- [77] F. Chen, L.L. Liu, J.J. Chen, W.W. Li, Y.P. Chen, Y.J. Zhang, J.H. Wu, S.C. Mei, Q. Yang, H.Q. Yu, Efficient decontamination of organic pollutants under high salinity conditions by a nonradical peroxymonosulfate activation system, *Water Res.* 191 (2021), 116799, <https://doi.org/10.1016/j.watres.2020.116799>.
- [78] Y. Fan, Y. Zhou, L. Zhang, Y. Feng, K. Shih, Highly efficient catalysts of phytic acid-derivative cobalt phosphide encapsulated in N, P-codoped carbon for activation of peroxymonosulfate in norfloxacin degradation, *Sep. Purif. Technol.* 264 (2021), 118367, <https://doi.org/10.1016/j.seppur.2021.118367>.
- [79] H. Meng, C. Nie, W. Li, X. Duan, B. Lai, Z. Ao, S. Wang, T. An, Insight into the effect of lignocellulosic biomass source on the performance of biochar as persulfate activator for aqueous organic pollutants remediation: epicarp and mesocarp of citrus peels as examples, *J. Hazard. Mater.* 399 (2020), 123043, <https://doi.org/10.1016/j.jhazmat.2020.123043>.